



D2.1 Sea Ice Thickness Algorithm Theoretical Basis Document (ATBD)

Doc Ref: SICCI-P2-ATBD(SIT)

Version: 1.0

Date: 25 September 2017



Change Record

Issue	Date	Reason for Change	Author(s)
1.0	25 September 2017	Fist Issue of SIT ATBD for Phase 2	Stephan Paul Stefan Hendricks Eero Rinne

Authorship

Role	Name	Signature
Written by:	Stephan Paul (AWI) Stefan Hendricks (AWI) Eero Rinne (FMI)	
Checked by:	Gary Timms	
Approved by:	Stein Sandven	
Authorised by:	Pascal Lecomte	

Distribution

Organisation	Names	Contact Details
ESA	Pascal Lecomte	Pascal.Lecomte@esa.int
NERSC	Stein Sandven, Kirill Khvorostovsky	Stein.Sandven@nersc.no; kirill.khvorostovsky@nersc.no
CGI	Gary Timms, Sabrina Mbajon, Clive Farquhar	gary.timms@cgi.com; sabrina.mbajon.njiche@cgi.com; clive.farquhar@cgi.com
MET Norway	Thomas Lavergne, Atle Sørensen	t.lavergne@met.no; atlems@met.no
DMI	Rasmus Tonboe	rtt@DMI.dk
DTU	Roberto Saldo, Henriette Skourup, Leif Toudal Pedersen	rs@space.dtu.dk; hsk@space.dtu.dk; ltp@space.dtu.dk
FMI	Marko Mäkynen, Eero Rinne	marko.makynen@fmi.fi; eero.rinne@fmi.fi;
University of Hamburg	Stefan Kern, Lars Kaleschke, Xiangshan Tian-Kunze	stefan.kern@zmaw.de; lars.kaleschke@uni-hamburg.de; xiangshan.tian-kunze@uni-hamburg.de
University of Bremen	Georg Heygster	heygster@uni-bremen.de
MPI-M	Dirk Notz	dirk.notz@mpimet.mpg.de
Ifremer	Fanny Ardhuin	Fanny.Ardhuin@ifremer.fr
AWI	Marcel Nicolaus, Stefan Hendricks, Thomas Hollands	marcel.nicolaus@awi.de; stefan.hendricks@awi.de; thomas.hollands@awi.de

Table of Contents

1	Introduction	7
1.1	Document Structure.....	7
1.2	Document Status.....	7
2	Sea Ice Thickness (SIT)	8
2.1	Overview	8
2.2	Additional/New Sensors.....	12
2.3	Filtering.....	15
2.4	Surface-Type Classification	15
2.5	Retracking	27
2.6	Envisat Backscatter Drift Correction	35
2.7	Radar Freeboard, Sea-Surface Height and Sea-Ice Freeboard.....	36
2.8	Sea-Ice Thickness.....	39
2.9	Uncertainties.....	40
3	References	45

List of Figures

Figure 2-1: Average winter (October to March) Arctic sea ice thickness in meters from October 1993 to March 2001 computed from pulse-limited ERS satellite altimeter measurements	8
Figure 2-2: Monthly mean sea ice thickness data (March 2011) computed from Envisat RA-2 satellite altimeter measurements.....	9
Figure 2-3: Monthly mean sea ice thickness data (March 2011) computed from CryoSat-2 satellite altimeter measurements.....	9
Figure 2-4: Flow chart for the Sea Ice Thickness Processor.....	11
Figure 2-5: SIT estimates from ERS-2 RA for March 1996.....	12
Figure 2-6: Comparison of Sentinel 3 and Cryosat-2 derived freeboards.....	14
Figure 2-7: Flowchart for the process of deriving thresholds for the new surface-type classification	17
Figure 2-8: Time-series of surface-type fractions for the sensor overlap period between CryoSat-2 (CS2) and Envisat RA-2 (ENV) for the Arctic	25
Figure 2-9: Time-series of surface-type fractions for the sensor overlap period between CryoSat-2 (CS2) and Envisat RA-2 (ENV) for the Antarctic.....	25
Figure 2-10: Visualizations of monthly sea-ice fraction, lead fraction, and valid fraction benchmarks for the Arctic (March 2012).....	26
Figure 2-11: Visualizations of monthly sea-ice fraction, lead fraction, and valid fraction benchmarks for the Antarctic (September 2011)	27
Figure 2-12: Visualizations of two monthly sets of figures (from left to right): Freeboard difference between Envisat RA-2 and CryoSat-2, the best achievable freeboard difference using an optimal retracker threshold, the sea-ice backscatter, the leading-edge width, and the iteratively estimated optimal threshold for November 2011 (top row) and March 2012 (bottom row)	28
Figure 2-13: Visualizations of averaged binned optimal threshold values on an x-y plane of leading-edge width and sea-ice backscatter for the Arctic. The blue plane is the 3 rd order polynomial fit through all data points	29
Figure 2-14: As Figure 2-12 but for the Antarctic showing May 2011 (top row) and September 2011 (bottom row)	31
Figure 2-15: As Figure 2-13 but for the Antarctic and captured from two different viewpoints.	31
Figure 2-16: Mean freeboard for each month of the sensor overlap period (top) for Envisat RA-2 (red) and CryoSat-2 (blue) and the corresponding mean freeboard difference between both sensors in centimetres (middle) and percent with reference to CryoSat-2 (bottom) for the Arctic	33
Figure 2-17: Setup as in Figure 2-16 but for the Antarctic	34

Figure 2-18: Scatterplot of all gridded freeboard estimates of CryoSat-2 (y-axis) vs. Envisat RA-2 (x-axis) for the Arctic (left) and the Antarctic (right)..... 35

Figure 2-19: Visualizations of the monthly averaged sea-ice backscatter reduction between 2002 and 2012 over ocean-type waveforms obtained between 70°N-75°N and 40°E-50°E 36

Figure 2-20: Hillshaded sea surface height of the DTU15 global mean sea surface height product for the SIT ECV target region in the northern and southern hemisphere.. 37

Figure 2-21: Computation of radar freeboard 38

Figure 2-22: Example from along-track CryoSat-2 freeboard retrieval. a) Orbit location, b) surface type classification with classes unknown, lead and sea ice with percentage and geographical location along track c) Lead detections, mean sea surface height and sea surface height anomaly d) unfiltered radar freeboard 38

Figure 2-23: Computation of sea-ice thickness 40

Figure 2-24: Example of Sea Surface Height Uncertainty 41

Figure 2-25: Gridded uncertainties (Example CryoSat-2 March 2015 Arctic data) 44

List of Tables

Table 2-1: Summary of used auxiliary data sets	10
Table 2-2: The table lists the latitudinal boundaries for the northern and southern hemisphere used for the region filtering	15
Table 2-3: Metrics for ocean surface-type classification of waveform data for all sensors, hemispheres, and radar modes	19
Table 2-4: Metrics for lead surface-type classification of Envisat RA-2, CryoSat-2 SAR mode, and CryoSat-2 SIN mode waveform data for the Arctic.....	20
Table 2-5: Metrics for sea-ice surface-type classification of Envisat RA-2, CryoSat-2 SAR mode, and CryoSat-2 SIN mode waveform data for the Arctic.....	21
Table 2-6: Metrics for lead surface-type classification of Envisat RA-2, CryoSat-2 SAR mode, and CryoSat-2 SIN mode waveform data for the Antarctic	22
Table 2-7: Metrics for sea-ice surface-type classification of Envisat RA-2, CryoSat-2 SAR mode, and CryoSat-2 SIN mode waveform data for the Antarctic	24
Table 2-8: Overview of uncertainty sources for sea ice freeboard and thickness retrieval	40

1 Introduction

1.1 Document Structure

This document describes in detail the Algorithm Theoretical Basis for the Sea Ice Essential Climate Variables products to be produced in ESA's Climate Change Initiative. In addition to the new developments, the document includes the ATBDv0, ATBDv1 and ATBDv2 contributions for the Sea Ice Thickness (SIT) aspects.

1.2 Document Status

This is the first issue of the ATBD document for Phase 2 of the Sea Ice CCI project. The document describes all the algorithms used for the comparison, the chosen in RRDP exercise algorithms and the processing steps for obtaining the final sea ice thickness data set.

The description of the SIT retrieval algorithm reflects the state at the beginning of the Phase 2 of the SICCI project and will need to be updated after the SIT production system has been validated and finalized. Especially a consistent formulation of the computation of freeboard and thickness uncertainty will only be available in the final version of the SIT algorithm.

2 Sea Ice Thickness (SIT)

2.1 Overview

This part of the document is intended as a generic guide to setting up a sea ice thickness processing system for any polar orbiting satellite radar altimeter. The general method is described and specific examples are given. The general processing system is identical for pulse-limited as well as for SAR altimetry. Any sensor type specific differences are stated.

The method used to extract sea ice thickness from radar altimetry data is heavily based on the pioneering method used for ERS-2 [Peacock and Laxon, 2004; Laxon et al., 2003]. The method involves separating the radar echoes returning from the ice floes from those returning from the sea surface in the leads between the floes. This step of a surface-type classification is crucial and allows for a separate determination of the ice floe and sea surface heights. The freeboard that is the elevation of the ice upper side (or ice-snow interface) above the sea level can then be computed by deducting the interpolated sea surface height at the floe location from the height of the floe. Sea-ice thickness can then be calculated from the sea-ice freeboard. Figure 2-1 shows an example of some results using this method taken from Laxon et al. (2003) for ERS data. Figure 2-2 and Figure 2-3 show a corresponding Arctic sea ice thickness map from Envisat RA-2 and CryoSat-2 data using the here presented algorithm.

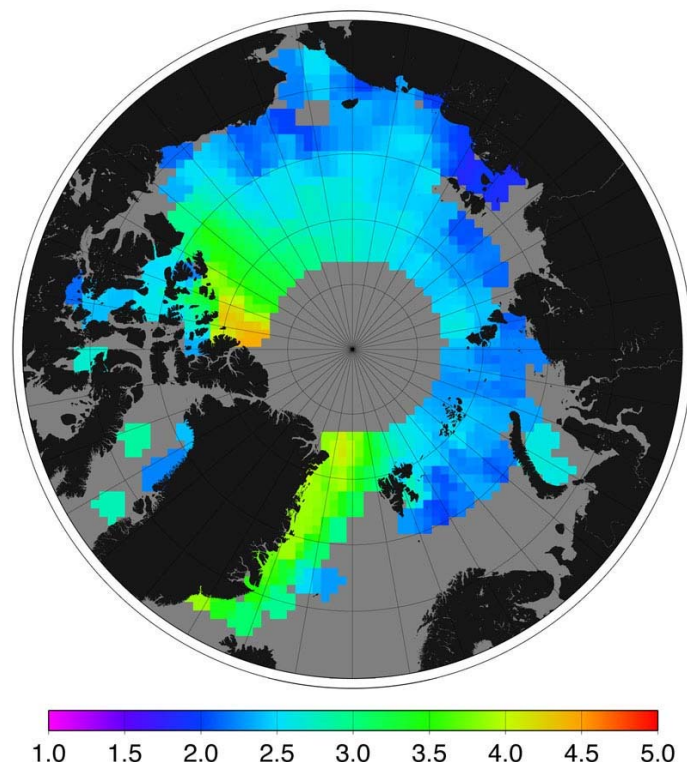


Figure 2-1: Average winter (October to March) Arctic sea ice thickness in meters from October 1993 to March 2001 computed from pulse-limited ERS satellite altimeter measurements

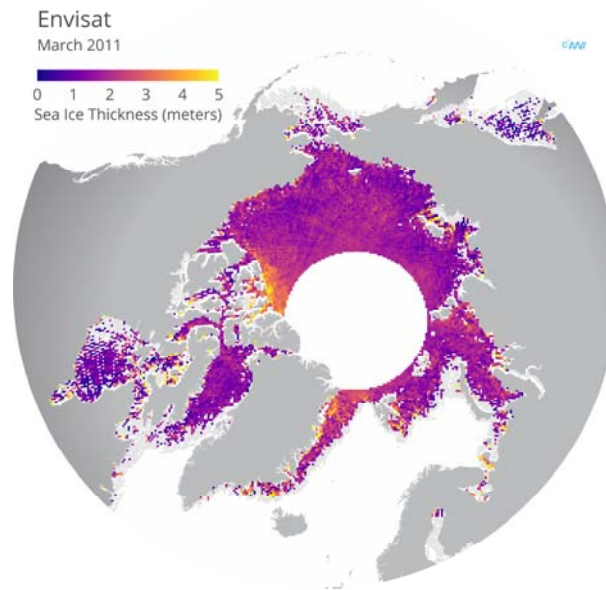


Figure 2-2: Monthly mean sea ice thickness data (March 2011) computed from Envisat RA-2 satellite altimeter measurements

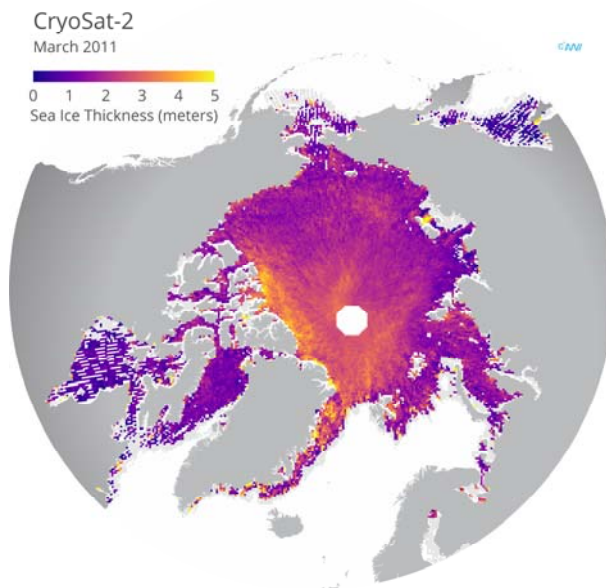


Figure 2-3: Monthly mean sea ice thickness data (March 2011) computed from CryoSat-2 satellite altimeter measurements

The input dataset must contain the radar echo waveforms and all other fields mentioned in this document such as altitude, range, atmospheric corrections and geophysical corrections. Figure 2-4 shows a flow chart for each step of the sea ice thickness processor. Each step is explained in detail in the sections below.

In case of Envisat RA-2, the input for the sea ice thickness processor is version 2.1 of the Envisat SGDR data. The SGDR data contains the waveforms as well as all other required fields. Each orbit is stored in two data files. The earlier of the two data files contains the data for the ascending arc from -81.5 latitude up to

+81.5 latitude, and the later of the two the descending arc from +81.5 latitude back down to -81.5 latitude. These files are read sequentially and the output split at appropriate points to make continuous Arctic and Antarctic passes.

For CryoSat-2, the current version of Baseline C orbit data files are used and separated into sections of different instrument modes by the processor. The SIRAL altimeter is operated in two different modes over sea ice: a) In synthetic aperture radar (SAR) off-coast and b) in synthetic aperture radar interferometric (SIN) mode to enable more accurate land ice altimeter measurements with higher surface slopes. For the product generation both data products are used. In addition to the different altimeter type that improves the spatial resolution, the higher orbit inclination of CryoSat-2 allows sea ice thickness measurements in the Arctic up to 88N.

The important intermediate step between the range measurement of the satellite and the estimated sea-ice thickness is freeboard. Here, the thickness retrieval algorithm is based on the assumption that for Ku-Band radar altimetry the backscatter of the snow layer is minor to the backscatter of the snow-ice interface. Thus, the radar altimeter is ranging to the snow-ice interface and providing an estimate of sea ice freeboard above the local sea level. Laser altimetry instead is based on ranging to the top snow surface. In case of non-negligible snow backscatter or absorption, the estimate of sea ice freeboard by radar altimeters is likely to be biased high. However, even if the radar range estimate penetrates the snow cover to the snow-ice interface, the slower wave propagation speed in the snow requires a geometric correction. Freeboard estimates, for which this correction has not been applied, are therefore termed radar freeboard.

The conversion into sea-ice freeboard requires either the use of auxiliary input data or a parametrization of snow depth. For the Arctic, we make use of the Warren snow climatology. As the Warren climatology is based on data sets obtained from Arctic drift stations in regions of multi-year sea ice (MYI), snow-depth values are suspected to be biased high over first-year sea-ice (FYI).

In order to discriminate between FYI and MYI in the Arctic, we use a MYI fraction data set based on the Special Sensor Microwave Imager (SSM/I)/Special Sensor Microwave Imager Sounder (SSMIS) sensors on-board of the Defense Meteorological Satellite Program (DMSP) satellites provided by the Integrated Climate Data Center (ICDC). Using this MYI fraction data set and following Kurtz et al. (2011), we apply a correction to the Warren climatology over FYI. This correction is a linear proportional reduction of the original snow depth with the present FYI fraction down to 50 % of its original value over pure FYI.

Parameter	Envisat RA-2 Arctic	Envisat RA-2 Antarctic	CryoSat-2 Arctic	CryoSat-2 Antarctic
SIC	OSI-SAF-409	OSI-SAF-409	OSI-SAF-409/430	OSI-SAF-409/430
SIT	ICDC MYIfrac	Single Ice Type	ICDC MYIfrac	Single Ice Type
Snow Depth	Warren99 scaled	AMSR-E/2 climatology	Warren99 scaled	AMSR-E/2 climatology
Snow Density	Warren99	fixed/clim	Warren99	fixed/clim
MSS	DTU15	DTU15	DTU15	DTU15

Table 2-1: Summary of used auxiliary data sets

For the Antarctic, we assume only a single sea-ice type being present. As the Warren climatology is only available for the Arctic, we use a snow-depth climatology derived from Advanced Microwave Scanning Radiometer-EOS (AMSR-E) and AMSR-2 data for the Antarctic. This data set is based on a revised version of the approach described by Markus and Cavalieri (2013) and provided by the ICDC.

Other required auxiliary input data sets for the estimation of sea ice freeboard and sea ice thicknesses comprise the use of the sea-ice concentration (SIC) data obtained from the Ocean and Sea Ice Satellite Application Facility (OSISAF) for both hemispheres, as well as the mean sea-surface height product provided by the Danish Technical University (DTU) in its 2015 version.

A summary of all used auxiliary data sets for the production of the sea-ice thickness climate data record is presented in Table 2-1.

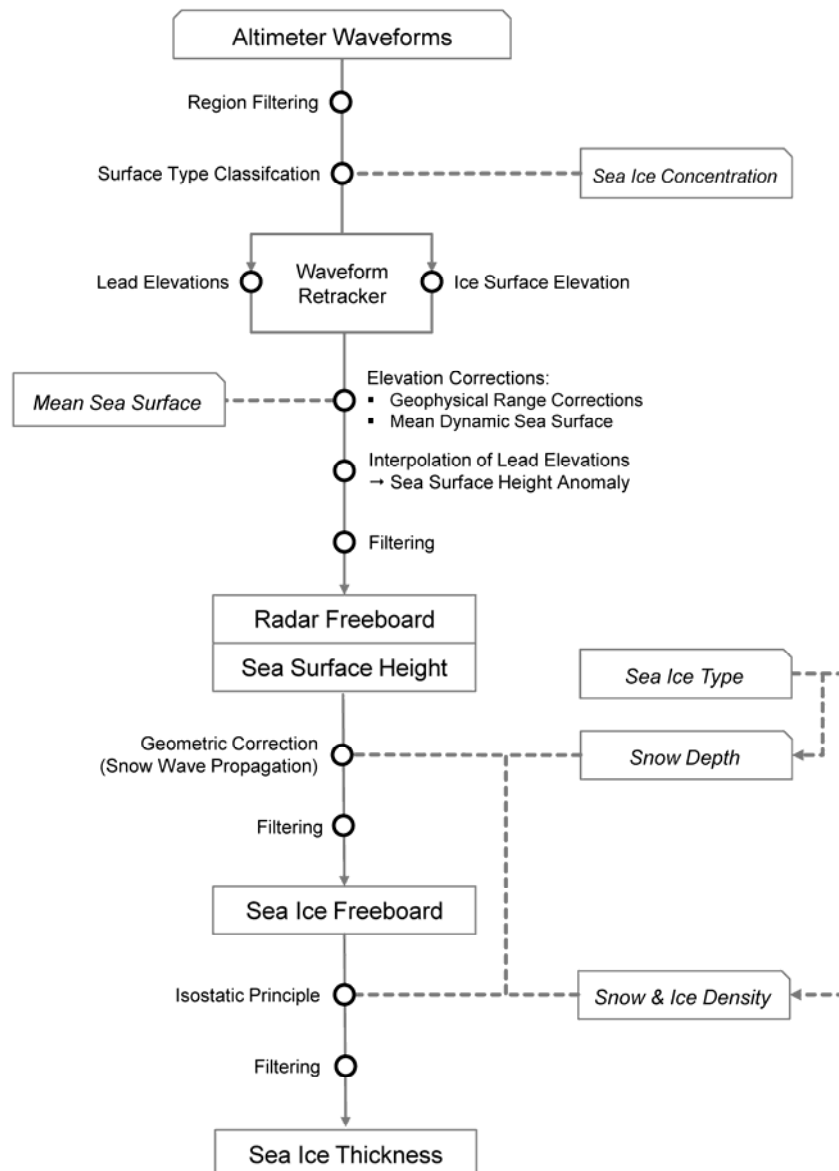


Figure 2-4: Flow chart for the Sea Ice Thickness Processor

Figure 2-4 presents an overview about the sea-ice thickness processing chain. In the following sub chapters first some general filtering steps for each sensor are described. Afterwards, the different processing steps, starting with the surface-type classification, are described and necessary thresholds/coefficients are summarized for Envisat RA-2 as well as for CryoSat-2. This continues with a thorough description of the range retracking procedure and a necessary Envisat RA-2 backscatter correction. Furthermore, the processing chain of radar freeboard and sea-surface height derivation, the estimation of sea-ice freeboard, and the estimation of sea-ice thickness are described. In a final step, the various calculated uncertainties are described.

2.2 Additional/New Sensors

The current CCI processing has been implemented for Envisat RA-2 and Cryosat-2 SARAL2. This section discusses the available altimeter missions and their usability for extending the CCI CRDP product.

Due to the toolbox nature of PySiral, the task of adding support for new sensors to the software is reasonably straightforward. However, the main challenge is bringing the quality of the SIT product up to CRDP standards as well as ensuring the consistency with already implemented sensors. For EnviSat RA2 and CryoSat-2, combining traditional pulse-limited delay-doppler altimetry turned out to require a significant scientific effort which resulted in the algorithm described in this document. We expect the effort of extending the CRDP with ERS-1/2 and Sentinel-3 (S3) - ERS towards the past, S3 in the future - to be a more simple task, but not a trivial one.

2.2.1 ERS-1/2

The EnviSat RA2 style reprocessed ERS-1/2 product has been released by the ESA REAPER project. We calculated the SIT estimates with the EnviSAT processing scheme for several test months. The result for March 1996 (ERS-2) is presented in Figure 2-5.

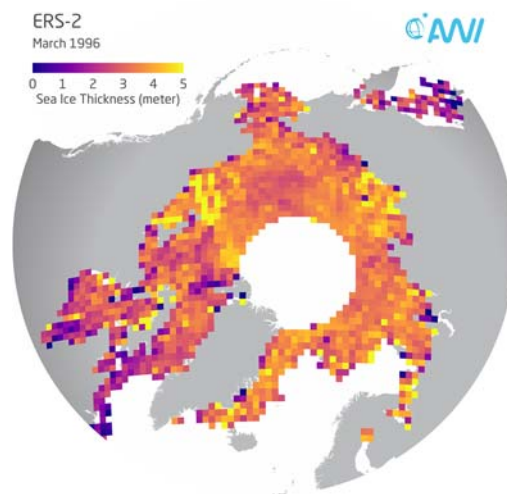


Figure 2-5: SIT estimates from ERS-2 RA for March 1996

For ERS-2, we find the overall spatial distribution, as well as the magnitude, of freeboard and SIT to differ from the one shown by EnviSat and CryoSat-2. Overall, the SIT is unrealistically large and the signal is noisier than expected. This is most likely due to us not being able to carry out the processing step Peacock and Laxon (2004) call "pulse blurring correction". This is a processing step unique to ERS altimeters, removing the "blurring" of waveforms due to waveforms to be averaged not being perfectly aligned. Despite our efforts, we could not find the variables required to do the deblurring in the style of Peacock and Laxon (2004) in the REAPER data. Specifically we could not find the values of height tracking loop error signal ϵ . However, the addition of ERS-1&2 data to the CRDP is the next logical step, since that will extend the current time series considerably. However, this will require looking further into the Level 1B processing of ERS waveforms and must be done in close collaboration with the REAPER project.

2.2.2 Sentinel3

S3 is a European satellite mission providing continuation of the sea related measurements of Envisat. It carries, in addition to other instruments, a delay-doppler altimeter SRAL much akin to the SIRAL onboard Cryosat-2. The drawback of S3 is the inclination its orbit (98,750, same as Envisat) in comparison to Cryosat-2 which provides coverage considerably closer to the North Pole. Still, the S3 will be the best option to continue the CRDP into the future for several reasons. Firstly, S3 will be a constellation of satellites with continuation guaranteed past the lifetime of one single platform. The S3A satellite, first of the series of four, already provides data overlapping with Cryosat-2, something that is not secured with ICESat-2 which is still to be launched. Lastly, the S3 processing is already implemented in PySiral to a prototype degree.

First experiments with S3A SIT processing show overall good agreement with Cryosat-2 (see Figure 2-6). The S3A freeboards are however somewhat higher than those of Cryosat-2. These are due to high outliers on the processed freeboard. One of the potential culprits for these outliers is the lack of zero-padding and using Hamming window in the L1 processing of S3, which results sidelobe artefacts to carry all the way to the 20 Hz waveforms. However, further work (namely FB processing with and without applying zero-padding and Hamming window in the L1 processing) must be carried out to confirm this hypothesis. Similarly, the surface classification thresholds must be set for S3A so that the result is consistent with Cryosat-2. These remain as future work.

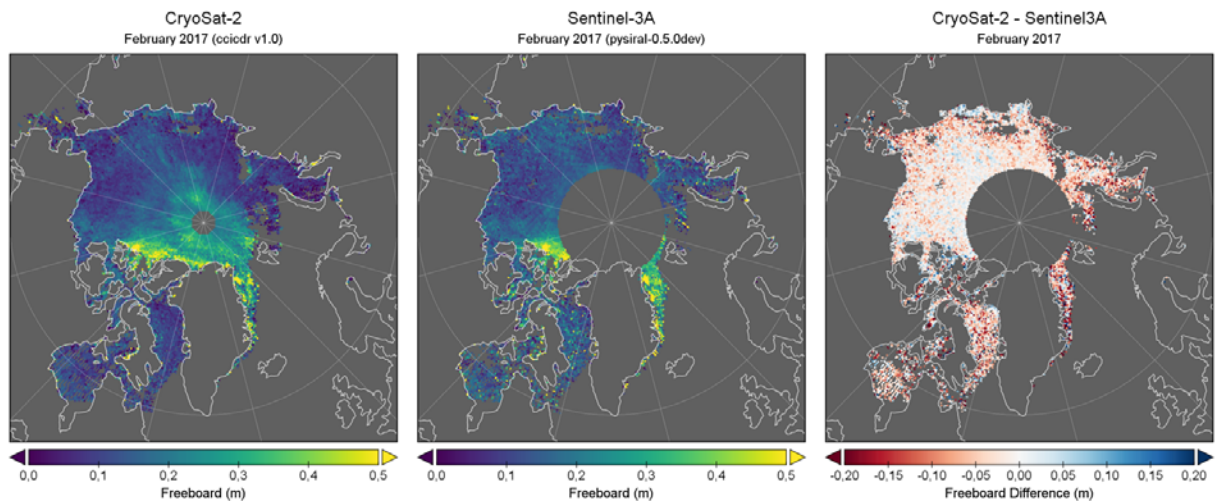


Figure 2-6: Comparison of Sentinel 3 and Cryosat-2 derived freeboards

2.2.3 HY-2

The Chinese HY-2 satellite carries a traditional pulse limited radar altimeter that is heritage of the Envisat RA-2 (Dong et al 2004). The data should, in principle, be possible to use for sea ice freeboard processing much in the same style as the Envisat data. However, due to lack of access to the data and documentation, HY2 has not been implemented in PySiral. However, if in the future we get access to the data and documentation, adding at least preliminary support should be a reasonable task. After this the quality of the data can be assessed.

2.2.4 AltiKa

Currently, there are ongoing projects, such as the ESA ARCTIC+ Snow on Sea Ice, with the aim to derive snow thickness over sea ice using coincident AltiKa and Cryosat-2 observations. Due to slightly higher operating frequency, combining freeboard and thickness estimates from AltiKa with EnviSat and Cryosat-2 estimates will most likely be complicated. Thus the biggest contribution towards the future CCI programme lies in the snow estimates derived using AltiKa data.

2.2.5 ICESat-1 and ICESat-2

ICESat-1 and ICESat-2 are laser altimeter missions, past and future respectively, that provide estimates of sea ice freeboard and thickness. The role of ICESat-1 in the CCI project has been to provide independent validation data for uncertainty estimation as well as algorithm development. When ICESat-2 will be successfully launched, discussion should take place if it will be used primarily for similar purposes as its predecessor, or should it be used as a data source for future CRDP.

To allow formal comparisons of ICESat-1 and radar altimeters, preliminary support of ICESat-1 data has been implemented in PySiral. This allows for example using the same auxiliary data (sea ice concentration, MSSH, etc.) for both ICESat-1 and other missions.

2.2.6 Other past Radar Altimeters

In addition to the ones mentioned above, there have been several radar altimeter missions, such as Seasat, Geosat and the Jason series, with the specific focus on the world oceans. These altimeters have, unfortunately for the application of measuring sea ice, flown at orbits with little or no coverage at the high latitudes where sea ice is usually found. In consequence, they are not valuable additions to the CRDP of sea ice CCI.

2.3 Filtering

2.3.1 General Filtering

There is some sensor-specific general filtering applied, which follows UCL's implementation of the Envisat algorithm used during phase 1. This filtering is based on the available flags in the Envisat data indicating any significant problems with any record. In UCL's implementation of the filtering for Envisat, the Measurement Confidence Data Flags (MCD Flags) in the SGDR data are examined for problem records. We remove records where the following flags are raised: 0 (Packet Length Error), 1 (OBDR invalid), 4 (AGC Fault), 5 (Rx Delay Fault) and 6 (Waveform Fault).

For CryoSat-2 level-1b data, no general filtering mechanisms are necessary.

2.3.2 Region Filtering

The latitudinal boundaries within which Arctic and Antarctic sea ice is found are listed in the Table 2-2. The latitude values in the satellite data are examined and any data points outside these regions are rejected from the processing. The surface type flag in the data is also examined and any data not flagged as over ocean is also rejected.

	Minimum Latitude	Maximum Latitude
Arctic	60.0	90.0
Antarctic	-90.0	-50.0

Table 2-2: The table lists the latitudinal boundaries for the northern and southern hemisphere used for the region filtering

2.4 Surface-Type Classification

The surface-type classification is a crucial part in the processing chain of deriving sea-ice freeboard (and therefore sea-ice thickness), as the detection of leads is pivotal for determining the sea-surface height. The sea-surface height in turn is used as the reference from which the sea-ice freeboard is calculated. Additionally, a clear distinction between leads, sea ice and ambiguous mixed signals (which will be excluded from the actual freeboard retrieval) helps to improve the quality and accuracy of resulting sea-ice freeboard estimates. In other words, a surface-type

selection bias is very likely to also have an impact on the resulting sea-ice freeboard and hence also the sea-ice thickness.

In general, with smaller instrument footprint sizes, less surface-type mixing occurs. However, leads often dominate acquired waveforms due to their specular reflection, and therefore act as sources of strong off-nadir backscatter signals. These off-nadir leads can substantially decrease the quality of the range retracking and increase the sensors' footprint. This is especially true for pulse-limited radar altimeters. In case of Envisat RA-2, the nominal circular footprint of 2 km in diameter [Connor et al., 2009] can increase to up to 10 km [Chelton et al., 2001] for strong off-nadir backscatter sources. Despite its much smaller footprint (1.65 km × 0.30 km), Cryosat-2 can also be affected by off-nadir leads, which will result in erroneous freeboard estimates [Armitage and Davidons, 2014].

2.4.1 Procedure Description

In contrast to phase 1 of the ESA sea ice CCI, where a single threshold classification scheme for Envisat RA-2 was used along-side a multi-parameter classification scheme for CryoSat-2, we aim for a sensor consistent surface-type classification scheme for Envisat RA-2 and CryoSat-2. Therefore, a set of classifiers is necessary that is available for both sensors. Here, we use the sea-ice backscatter (SIG0), the leading-edge width (LEW) and the pulse peakiness (PP) as classifiers to positively identify between lead-type and sea-ice-type from otherwise ambiguous-type waveforms.

The pulse peakiness is subtly differently defined compared to the one used during phase 1 for Envisat RA-2 and follows the definition of Ricker et al. (2014):

$$PP = \sum_{i=1}^{N_{wf}} \frac{\max(WF)}{WF_i} \cdot N_{wf}$$

The leading-edge width is defined as the width in range bins along the power rise to the first maximum between 5 % and 95 % of the first-maximum peak power while using a ten-times oversampled waveform.

The choice for using three classifiers also allows for less strict thresholds compared to the previously used single threshold parameter classification for Envisat RA-2 during phase 1.

Over the course of a winter season, ice conditions can change substantially. Similar to leads, young and thin-ice areas feature rather specular reflections compared to other ice types. Furthermore, the amount of leads varies seasonally and regionally. Based on fixed thresholds for a whole winter season, these changes are difficult to capture and the rejection rate is increased unnecessarily. Hence, we decided on using monthly thresholds to improve the overall results and data quality.

There is a general lack of ground-truth data as collocated measurements of the same sea-ice situation are very difficult due to sea-ice drift and therefore rare. However, received waveforms feature very distinct characteristics and are well described in literature for sea ice and leads. These characteristics can also be deduced from the chosen set of classifiers. In order to bypass the lack of ground-

truth, we decided to use a combination of unsupervised clustering and supervised classification.

Based on this combination, we are able to determine suitable thresholds for data acquired by Envisat RA-2 as well as Cryosat-2. The work flow of how we derived the surface-type thresholds is summarized in Figure 2-7.

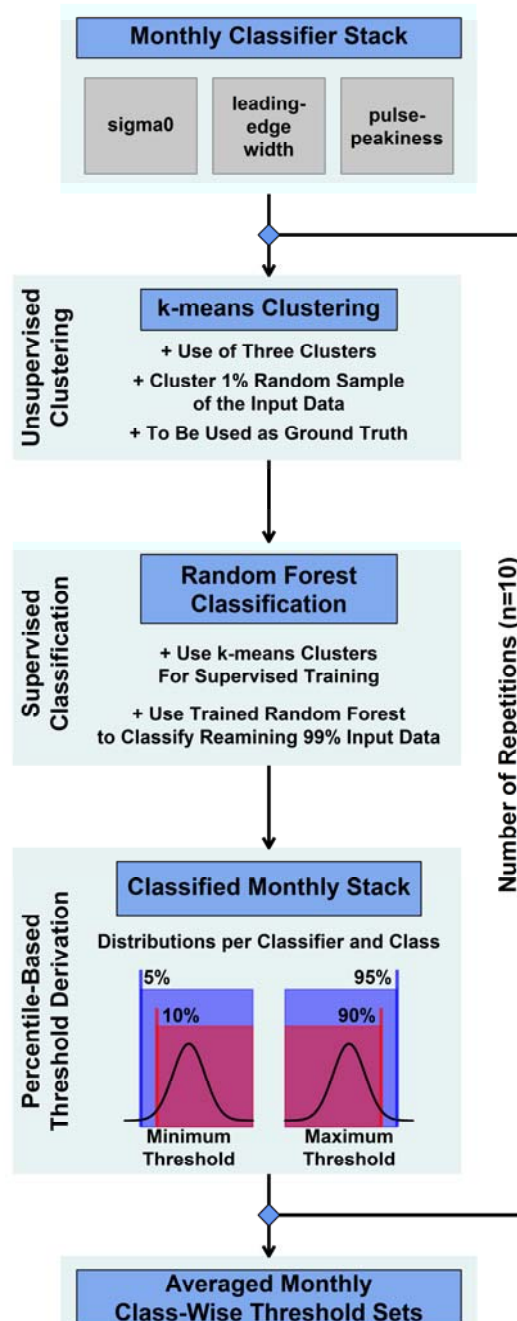


Figure 2-7: Flowchart for the process of deriving thresholds for the new surface-type classification

In a first step, the three classifiers are computed for all available L1b data per sensor and month in the sensor overlap period from November 2010 to March 2012. We only use waveforms that are located between 70°N and 81.5°N for the Arctic, are obtained over the ocean, and feature a minimum sea-ice concentration of 70%. The northern limit of 81.5°N was chosen to assure a maximum of consistency between Envisat RA-2 and CryoSat-2. In order to retrieve thresholds for the "Wingham Box" and other Arctic areas that are covered while CryoSat-2 operates in SIN mode, all waveforms above 70°N were used. For the Antarctic the same parameters apply, but waveforms are geographically limited to an area south of 65°S.

Next, 1 % of this monthly data are sampled randomly. This data sample is then separated into three clusters using k-means clustering [MacQueen et al., 1967; Hartigan et al., 1979]. This methodology is widely used to separate input data of N observations into K clusters of equal variance, whereby the within-cluster sum-of-squares are minimized [MacQueen et al., 1967; Hartigan et al., 1979].

Generally, the preselection of the number of clusters can be a problem when utilizing k-means clustering. However, while we also tested a higher number of initial clusters with perspective of later reunion of very similar clusters, a separation into just three classes turned out to be sufficient. Overall, lead waveforms account for a smaller fraction of the total measurements compared to sea-ice waveforms. Because of that and the fact that k-means clustering generally tends toward generating equal-size clusters (this is generally a presumption of k-mean algorithms), sole use of k-means clustering for the complete data set was not feasible.

This information in mind, the clustered 1 % data sample is therefore used as training data to train a random forest [Breiman, 2001]. Random forests are an ensemble machine learning method used for classification and are based on a large number of single decision trees that are fitted to randomized sub samples of the given training data set [Breiman, 2001]. After initial training, the random forest can then be used for classification of the remaining data. Each tree in the trained forest then does a classification and casts a unique vote. In the end, the majority decides the resulting class. Each decision tree is thereby grown following certain rules: First, from the training data of size N , N cases are sampled randomly with replacement as specific training data set for each single tree. Second, for M input parameters (in our case sea-ice backscatter, pulse peakiness, and leading-edge width), a fixed number $m \ll M$ of the given input parameters is specified and randomly selected out of M . The best split on these selected parameters m is then used to split the node. Throughout the growing of the forest, the value of m is held constant. Third, each tree is grown out fully, i.e., to its largest possible extent. No pruning is applied. In contrast to single decision trees that tend to overfit, random forests do not overfit and are also capable of dealing with unbalanced data sets [Breiman, 2001].

For the here-used classification problem, we always grow a total number of 500 decision trees per training. Due to the small number of input parameters ($M=3$), we set m to one.

The trained random forest for each month is then used to classify the remaining 99 % of the corresponding monthly data. From this classified data set, distributions for each of the three classifiers for each month in the sensor overlap period are obtained. These distributions feature clear distinctions along each classifiers respective total range for each surface-type class (leads, sea ice, and ambiguous). Sea-ice backscatter is on average in the upper part of the range for the lead class and in the lower for the sea-ice class. Similar observations are

apparent for pulse peakiness (upper part for leads, lower for sea ice) and leading-edge width (lower part for leads, upper part for sea ice). In other words, leads feature higher sea-ice backscatter and pulse peakiness as well as shorter leading-edge widths. The opposite is seen in the sea-ice class. The class of ambiguous signals is placed in between.

Thresholds are then obtained from the resulting classifier distributions by using either the 5 % or 10 % percentile for a minimum threshold, or the 90 % or 95 % percentile in case of a maximum threshold. The choice of using the more strict (10 %/90 %) or less strict (5 %/95 %) percentile thresholds depends on the sensor. Due to its larger footprint and therefore an expected higher degree of surface-type mixing, we chose the more strict thresholds for Envisat RA-2, and the less strict thresholds for CryoSat-2 due to its smaller footprint. For example, in order to derive thresholds for the detection of leads, the 5 %/10 % percentiles of the sea-ice backscatter and pulse-peakiness distributions would be used alongside the 90 %/95 % percentile of the leading-edge-width distribution.

The whole procedure, starting with randomly sampling 1 % from the initial monthly stack, is then repeated ten times. In a last step, the average minimum/maximum thresholds for each classifier, surface-type class, and month in the sensor overlap period are estimated. These thresholds are summarized in Table 2-3 through Table 2-7 and are used for all months in the complete climate data record.

Metric	Min	Max
Ocean waveforms are characterized by medium to low pulse peakiness (PP) values.		5
Only regions of very low ice concentration (SIC in %) values are suitable for the ocean surface type flag		5

Table 2-3: Metrics for ocean surface-type classification of waveform data for all sensors, hemispheres, and radar modes

Metric	Month	Envisat RA-2		CryoSat-2 SAR		CryoSat-2 SIN	
		Min	Max	Min	Max	Min	Max
Lead waveforms are characterized by strong pulse peakiness (PP)	JAN	46.90		67.30		264.30	
	FEB	46.40		66.30		257.90	
	MAR	46.20		66.60		253.60	
	APR	48.40		69.90		264.60	
	OCT	52.90		76.00		291.80	
	NOV	51.00		73.80		288.80	
	DEC	47.70		68.60		272.60	

Metric	Month	Envisat RA-2		CryoSat-2 SAR		CryoSat-2 SIN	
		Min	Max	Min	Max	Min	Max
Lead waveforms are also characterized by high backscatter values due to specular reflection (SIG0)	JAN	28.80		23.80		24.90	
	FEB	28.60		23.20		25.00	
	MAR	28.50		23.30		24.10	
	APR	28.40		23.40		24.50	
	OCT	32.80		28.00		29.00	
	NOV	30.80		25.80		27.40	
	DEC	29.30		24.10		25.80	
Lead waveforms feature a very steep increase in echo power and therefore short leading-edge widths (LEW)	JAN		0.82		0.77		1.10
	FEB		0.82		0.78		1.11
	MAR		0.82		0.78		1.13
	APR		0.82		0.76		1.09
	OCT		0.82		0.72		1.02
	NOV		0.82		0.73		1.03
	DEC		0.82		0.76		1.07
Only lead classifications by waveform are expected that fall into regions of sufficient ice cover (checked with SIC in %)	JAN	70		70		70	
	FEB	70		70		70	
	MAR	70		70		70	
	APR	70		70		70	
	OCT	70		70		70	
	NOV	70		70		70	
	DEC	70		70		70	

Table 2-4: Metrics for lead surface-type classification of Envisat RA-2, CryoSat-2 SAR mode, and CryoSat-2 SIN mode waveform data for the Arctic

Metric	Month	Envisat RA-2		CryoSat-2 SAR		CryoSat-2 SIN	
		Min	Max	Min	Max	Min	Max
Sea-ice waveforms shouldn't be peaky and therefore have a low pulse peakiness (PP)	JAN		16.00		30.50		99.40
	FEB		14.80		28.70		94.20
	MAR		14.10		28.10		89.90
	APR		14.20		28.50		90.00
	OCT		19.40		35.40		114.40
	NOV		19.30		34.90		113.90
	DEC		16.90		31.90		103.80
Sea-ice waveforms are also characterized by low backscatter values due to diffuse reflection (SIG0)	JAN	2.5	22.50	2.5	20.80	2.5	21.40
	FEB	2.5	21.80	2.5	19.90	2.5	20.90
	MAR	2.5	21.30	2.5	19.60	2.5	20.10
	APR	2.5	20.40	2.5	19.00	2.5	19.10
	OCT	2.5	25.90	2.5	25.70	2.5	24.30
	NOV	2.5	24.60	2.5	23.20	2.5	23.70
	DEC	2.5	22.80	2.5	21.10	2.5	22.00

Metric	Month	Envisat RA-2		CryoSat-2 SAR		CryoSat-2 SIN	
		Min	Max	Min	Max	Min	Max
Sea-ice waveforms feature a less steep increase in echo power and therefore longer leading-edge widths (LEW)	JAN	0.81		1.02			1.55
	FEB	0.83		1.08			1.58
	MAR	0.83		1.10			1.62
	APR	0.83		1.11			1.64
	OCT	0.78		0.91			1.44
	NOV	0.78		0.90			1.44
	DEC	0.80		0.97			1.51
Only sea-ice classifications by waveform are expected that fall into regions of sufficient ice cover (checked with SIC in %)	JAN	70		70		70	
	FEB	70		70		70	
	MAR	70		70		70	
	APR	70		70		70	
	OCT	70		70		70	
	NOV	70		70		70	
	DEC	70		70		70	

Table 2-5: Metrics for sea-ice surface-type classification of Envisat RA-2, CryoSat-2 SAR mode, and CryoSat-2 SIN mode waveform data for the Arctic

Metric	Month	Envisat RA-2		CryoSat-2 SAR		CryoSat-2 SIN	
		Min	Max	Min	Max	Min	Max
Lead waveforms are characterized by strong pulse peakiness (PP)	JAN	56.60		80.70		307.40	
	FEB	53.20		75.10		300.70	
	MAR	51.90		73.20		291.70	
	APR	50.70		69.50		288.50	
	MAY	50.10		69.70		283.70	
	JUN	49.30		69.30		284.20	
	JUL	49.50		69.20		276.90	
	AUG	49.10		69.50		284.40	
	SEP	49.30		69.70		278.90	
	OCT	51.60		71.70		289.40	
	NOV	53.90		76.00		299.40	
	DEC	55.10		78.10		307.70	

Metric	Month	Envisat RA-2		CryoSat-2 SAR		CryoSat-2 SIN	
		Min	Max	Min	Max	Min	Max
Lead waveforms are also characterized by high backscatter values due to specular reflection (SIG0)	JAN	33.20		28.50		29.20	
	FEB	32.10		26.80		29.00	
	MAR	31.80		26.20		28.50	
	APR	30.80		24.60		27.80	
	MAY	29.40		23.40		26.90	
	JUN	28.60		22.80		26.50	
	JUL	28.60		23.00		26.30	
	AUG	28.40		23.00		27.00	
	SEP	28.50		23.20		26.20	
	OCT	29.50		24.00		27.20	
	NOV	31.10		25.90		27.50	
	DEC	32.10		27.30		28.40	
Lead waveforms feature a very steep increase in echo power and therefore short leading-edge widths (LEW)	JAN		0.82		0.71		1.00
	FEB		0.82		0.73		1.01
	MAR		0.82		0.74		1.03
	APR		0.82		0.77		1.04
	MAY		0.82		0.77		1.06
	JUN		0.82		0.77		1.05
	JUL		0.82		0.78		1.07
	AUG		0.82		0.77		1.05
	SEP		0.82		0.77		1.07
	OCT		0.82		0.76		1.05
	NOV		0.82		0.74		1.02
	DEC		0.82		0.72		1.00
Only lead classifications by waveform are expected that fall into regions of sufficient ice cover (checked with SIC in %)	JAN	70		70		70	
	FEB	70		70		70	
	MAR	70		70		70	
	APR	70		70		70	
	MAY	70		70		70	
	JUN	70		70		70	
	JUL	70		70		70	
	AUG	70		70		70	
	SEP	70		70		70	
	OCT	70		70		70	
	NOV	70		70		70	
	DEC	70		70		70	

Table 2-6: Metrics for lead surface-type classification of Envisat RA-2, CryoSat-2 SAR mode, and CryoSat-2 SIN mode waveform data for the Antarctic

Metric	Month	Envisat RA-2		CryoSat-2 SAR		CryoSat-2 SIN	
		Min	Max	Min	Max	Min	Max

Metric	Month	Envisat RA-2		CryoSat-2 SAR		CryoSat-2 SIN	
		Min	Max	Min	Max	Min	Max
Sea-ice waveforms shouldn't be peaky and therefore have a low pulse peakiness (PP)	JAN		24.60		40.10		138.40
	FEB		20.70		35.30		126.10
	MAR		19.60		32.90		124.90
	APR		18.80		30.20		127.30
	MAY		17.50		28.70		122.20
	JUN		16.90		28.90		121.00
	JUL		16.60		28.10		114.90
	AUG		16.10		28.00		115.80
	SEP		16.30		28.40		114.30
	OCT		18.10		29.60		121.20
	NOV		20.70		34.10		126.50
	DEC		22.80		36.60		135.20
Sea-ice waveforms are also characterized by low backscatter values due to diffuse reflection (SIG0)	JAN	2.5	27.20	2.5	26.30	2.5	26.40
	FEB	2.5	25.40	2.5	24.10	2.5	25.10
	MAR	2.5	26.70	2.5	25.10	2.5	27.60
	APR	2.5	27.20	2.5	26.20	2.5	27.30
	MAY	2.5	24.60	2.5	23.10	2.5	24.90
	JUN	2.5	23.10	2.5	20.90	2.5	24.20
	JUL	2.5	22.50	2.5	20.20	2.5	24.10
	AUG	2.5	21.70	2.5	19.10	2.5	24.90
	SEP	2.5	22.30	2.5	20.00	2.5	23.70
	OCT	2.5	23.30	2.5	20.60	2.5	25.00
	NOV	2.5	25.20	2.5	22.90	2.5	25.20
	DEC	2.5	26.10	2.5	23.90	2.5	25.00
Sea-ice waveforms feature a less steep increase in echo power and therefore longer leading-edge widths (LEW)	JAN	0.78		0.87		1.31	
	FEB	0.80		0.95		1.40	
	MAR	0.80		0.98		1.37	
	APR	0.80		1.02		1.34	
	MAY	0.81		1.07		1.37	
	JUN	0.80		1.07		1.38	
	JUL	0.80		1.12		1.41	
	AUG	0.81		1.13		1.41	
	SEP	0.81		1.11		1.42	
	OCT	0.80		1.08		1.38	
	NOV	0.79		0.95		1.36	
	DEC	0.78		0.92		1.33	

Metric	Month	Envisat RA-2		CryoSat-2 SAR		CryoSat-2 SIN	
		Min	Max	Min	Max	Min	Max
Only sea-ice classifications by waveform are expected that fall into regions of sufficient ice cover (checked with SIC in %)	JAN	70		70		70	
	FEB	70		70		70	
	MAR	70		70		70	
	APR	70		70		70	
	MAY	70		70		70	
	JUN	70		70		70	
	JUL	70		70		70	
	AUG	70		70		70	
	SEP	70		70		70	
	OCT	70		70		70	
	NOV	70		70		70	
	DEC	70		70		70	

Table 2-7: Metrics for sea-ice surface-type classification of Envisat RA-2, CryoSat-2 SAR mode, and CryoSat-2 SIN mode waveform data for the Antarctic

2.4.2 Results

Utilizing this new and sensor-consistent surface-type classification scheme results in overall much better agreement between CryoSat-2 and Envisat RA-2 for typical benchmarks.

Compared to the surface-type classification used during Phase 1 for Envisat RA-2, our less strict approach allows for substantially more wave forms being classified as either lead or sea-ice type that were otherwise rejected before. Additionally, where there was a very high fraction of lead detections compared to only a very small fraction of classified sea-ice type waveforms during Phase 1, the spatial patterns and distributions of these occurrences are now better in line with what one would expect. Furthermore, the intermission consistency for the Arctic as well as the Antarctic has improved substantially (Figure 2-8 and Figure 2-9; Figure 2-10 and Figure 2-11)

The increased number of valid wave forms has an additional positive side effect on the overall data record: It allows for a much higher spatial resolution to be used in the final gridded Level 3 product without any compromises on overall coverage. Here, we are now able to provide a 25 km (50 km) resolution gridded data set for the Arctic (Antarctic) compared to a 100 km one during Phase 1.

Direct comparisons of surface-type class fractions (i.e., either ambiguous, lead, or sea ice) over the course of the sensor overlap period reveal an overall very good agreement between CryoSat-2 and Envisat RA-2 (Figure 2-8 and Figure 2-9). While the fraction of lead- and sea-ice waveforms is on average slightly smaller for Envisat RA-2 than for CryoSat-2 (about 8 % for the Arctic and 10 % for the Antarctic), both sensors show a similar seasonal development in both hemispheres.

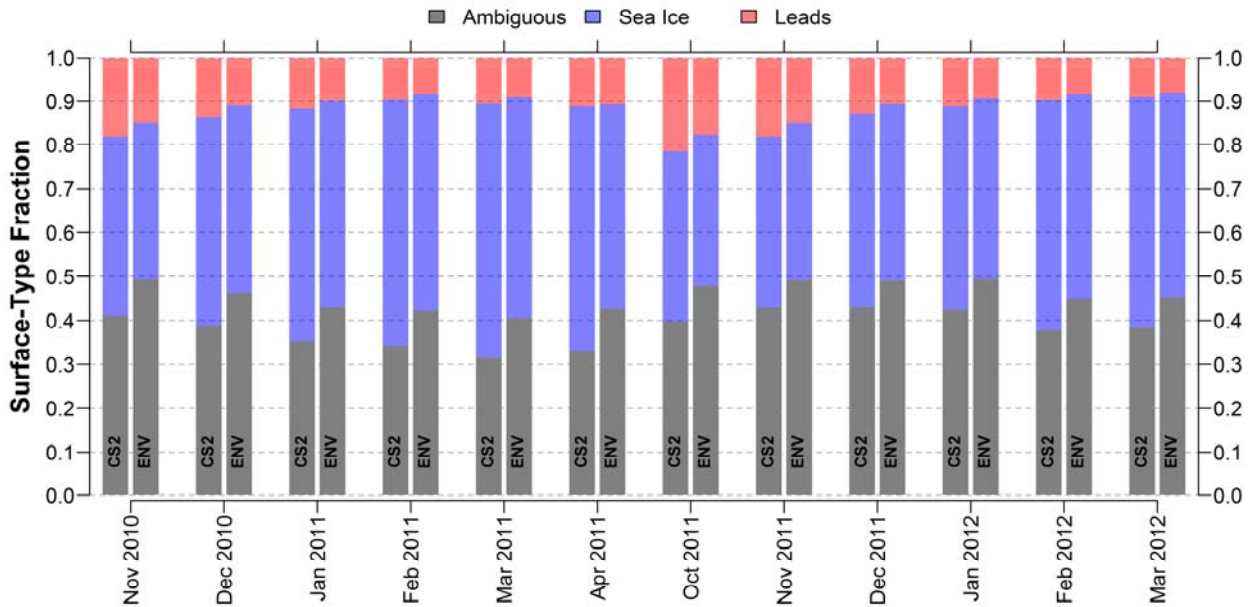


Figure 2-8: Time-series of surface-type fractions for the sensor overlap period between CryoSat-2 (CS2) and Envisat RA-2 (ENV) for the Arctic

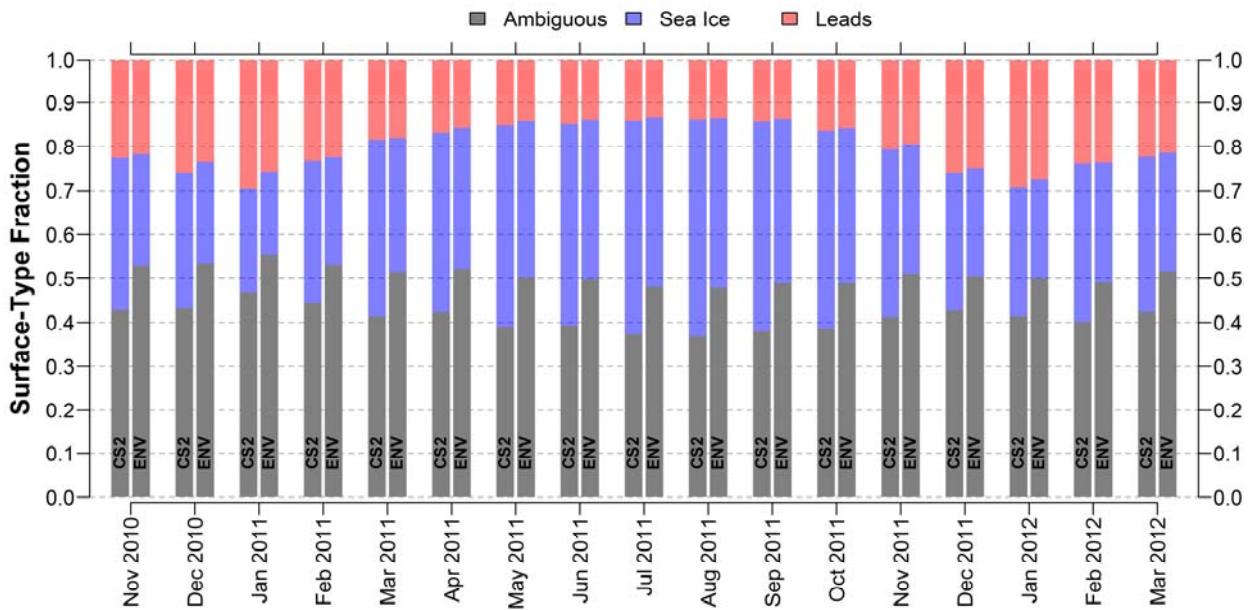


Figure 2-9: Time-series of surface-type fractions for the sensor overlap period between CryoSat-2 (CS2) and Envisat RA-2 (ENV) for the Antarctic

This seasonal change in the present sea-ice cover is also apparent from the derived surface-type class thresholds (Table 2-3 - Table 2-7). During summer months (Antarctic) and the early winter (Arctic), the number of lead waveforms is higher and returns from new and young ice tend to be more specular, which results in higher maximum thresholds in sea-ice backscatter and pulse peakiness. This observed seasonal shift in the distributions of the classifiers will also play an important role in the description of the new retracker scheme.

An exemplary visualization of monthly map-wise inter-comparisons between Envisat RA-2 and CryoSat-2 based on the benchmarks of valid-, lead-, and sea-ice fraction is shown in Figure 2-10. In these gridded data sets, the overall good agreement is confirmed. However, there are small differences, and as mentioned earlier, slightly smaller valid fractions for Envisat RA-2. This behavior is expected and results most likely from the much larger footprint of Envisat RA-2, especially in regions with high rates of sea-ice dynamics such as the Beaufort Sea, but also in the Laptev Sea. Here, the increased surface-type mixing likely prevents a clearer separation between waveform types.

Nevertheless, both comparisons highlight the overall good agreement that could be achieved between both sensors with this new surface-type classification scheme and the chosen settings during the sensor overlap period. These results therefore lay the foundation for a proper inter-mission sea-ice freeboard and sea-ice thickness data record.

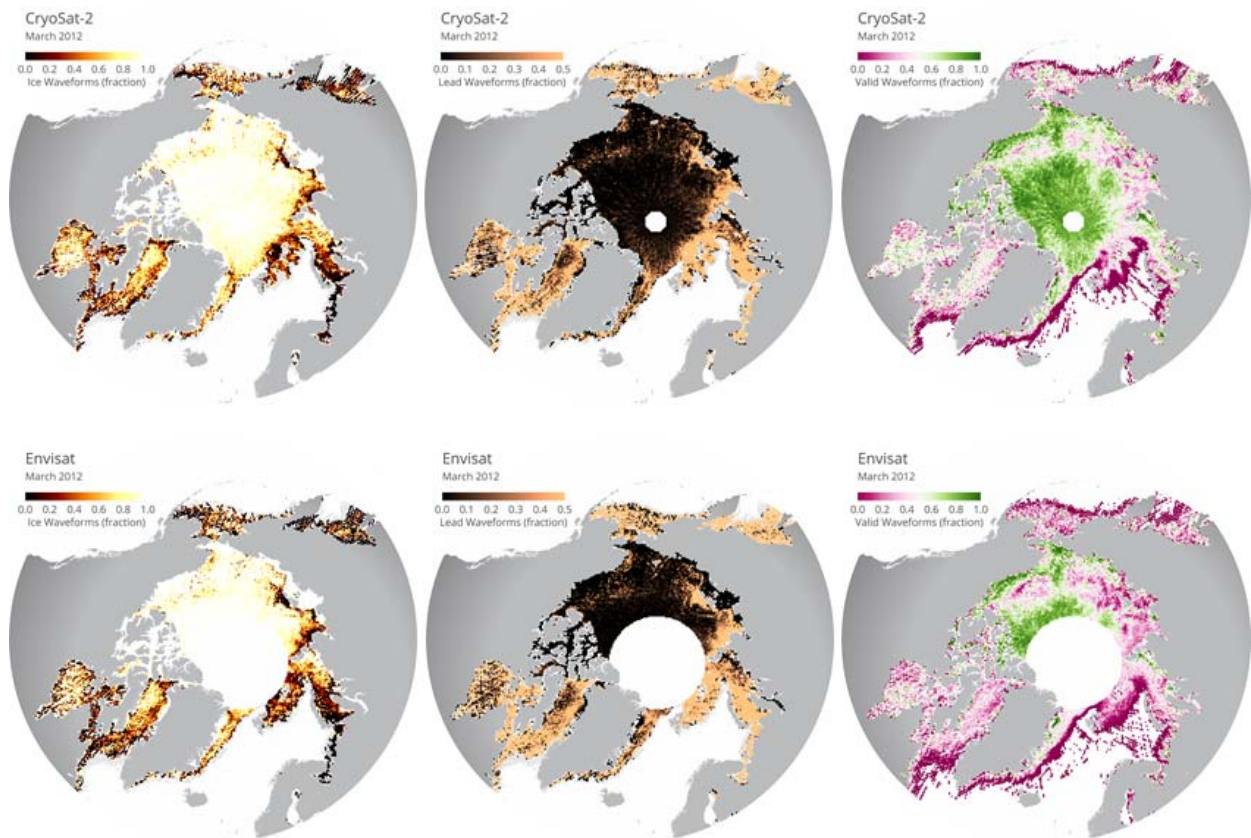


Figure 2-10: Visualizations of monthly sea-ice fraction, lead fraction, and valid fraction benchmarks for the Arctic (March 2012)

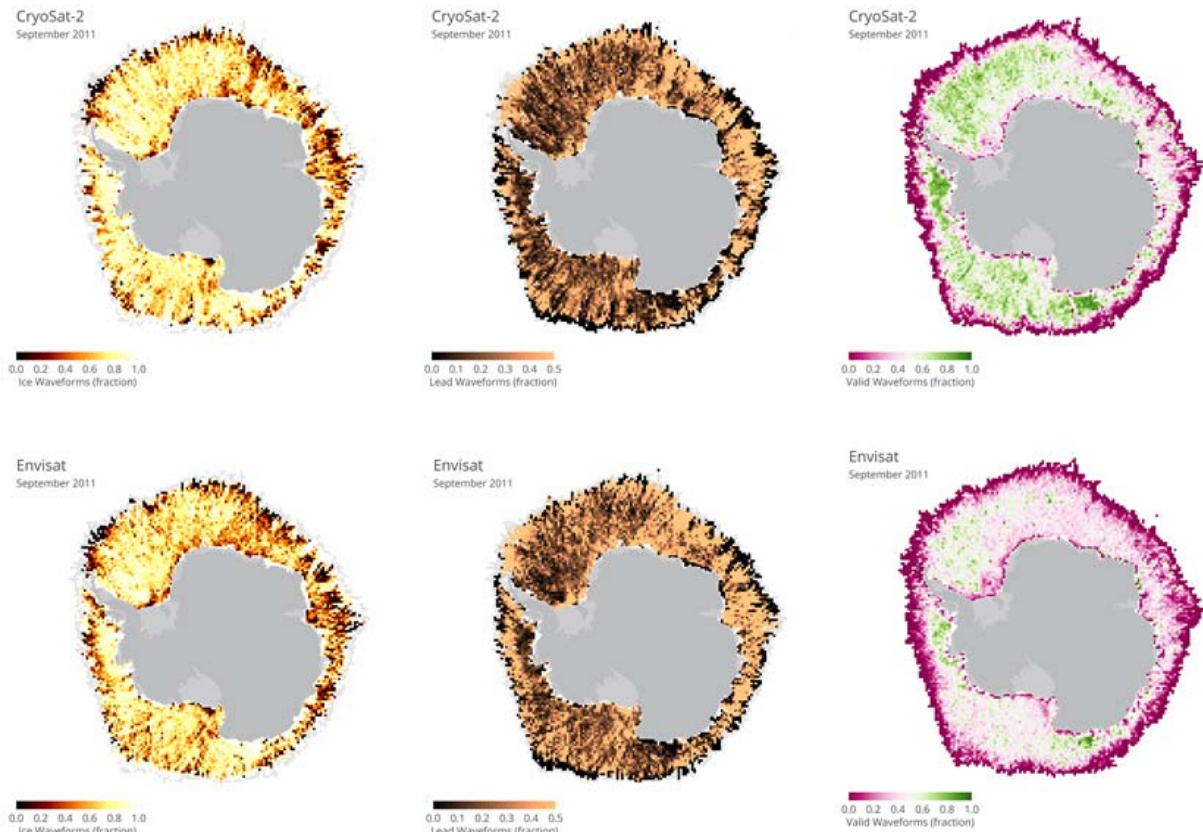


Figure 2-11: Visualizations of monthly sea-ice fraction, lead fraction, and valid fraction benchmarks for the Antarctic (September 2011)

2.5 Retracking

2.5.1 Procedure Description

The range retrieval algorithm for Envisat RA-2 and CryoSat-2 waveforms is identical for sea-ice and lead waveforms. Ocean waveforms are currently discarded. The used Threshold First Maximum Retracker Algorithm (TFMRA, Helm et al., 2014; Ricker et al, 2014) is based on the following steps:

- Estimate the noise level as the average of the first 5 bins of the waveform. However, in case of Envisat RA-2 we are following UCL's implementation and discard the counts in the first 5 bins of the echo as these just contain artefacts of the FFT.
- Oversampling of the echo waveforms by a factor of 10 using linear interpolation
- Smoothing of the oversampled waveform with a window filter size of 11 range bins
- Locating the first local maximum of the waveform: Must be higher than noise level + 15% of absolute peak power.

- e) Obtain the range value at a specified threshold of the power of the detected first maximum, by linear interpolation of the smoothed and oversampled waveform.

Continuing on the last point, the choice of retracker threshold is pivotal for the range estimation. Following AWI's implementation for CryoSat-2 (Ricker et al., 2014), we keep a consistent threshold of 50% from the first maximum peak power both for leads and sea-ice waveforms. For pulse-limited altimetry such as for Envisat RA-2, retracking near the maximum power for leads proved to be essential to retrieve reasonable freeboard estimates later on. Therefore, a threshold of 95% was chosen for leads from Envisat RA-2 waveforms. However, using a single fixed threshold of, e.g., 50% similar to CryoSat-2, results later on in sea-ice freeboard estimates that feature an overall smaller variation than CryoSat-2 estimates. Furthermore, expected thin-ice regions feature ice that is too thick and vice versa. We relate this behavior to the much larger footprint and the therefore increased mixing of surface types of different surface-roughness scales in every Envisat RA-2 waveform.



Figure 2-12: Visualizations of two monthly sets of figures (from left to right): Freeboard difference between Envisat RA-2 and CryoSat-2, the best achievable freeboard difference using an optimal retracker threshold, the sea-ice backscatter, the leading-edge width, and the iteratively estimated optimal threshold for November 2011 (top row) and March 2012 (bottom row)

From Figure 2-12 it appears that differences in sea-ice freeboard are related to differences in the waveform parameters of sea-ice backscatter and leading-edge width (as well as pulse peakiness, which is strongly correlated with sea-ice backscatter, but is not shown here). Areas of potential multi-year ice near the Canadian Archipelago and areas influenced by multi-year ice export are in general substantially too thin (e.g., about 20 cm and more in March), whereas areas of predominantly first-year sea ice are in general too thick in the Envisat RA-2 data. However, the level of freeboard difference appears to be seasonal, where Envisat RA-2 appears to be unable to keep track of these seasonal changes.

As these differences in sea-ice freeboard between CryoSat-2 and Envisat RA-2 appear to be indeed strongly correlated to patterns in the sea-ice backscatter and the leading-edge width of Envisat RA-2 waveforms, we decided to apply a tuning scheme by computing an adaptive range retracker threshold as a function of sea-ice backscatter and the leading-edge width to mitigate the differences. Due to the already mentioned larger footprint of Envisat RA-2 and hence increased mixing of different surface types, it appears to be necessary to treat waveforms differently

according to the wave-form shape (and hence surface properties) by means of retracking the main scattering horizon.

In order to derive the functional relationship between threshold and sea-ice backscatter/leading-edge width, we first processed all Envisat RA-2 for the complete sensor overlap period. This processing was done using the TFMRA with a fixed threshold for leads of 95 % and a threshold for sea-ice waveforms that was changed in each run. This sea-ice threshold ranged between 5 % and 95 % in steps of 5 %. For example, in the first run the complete data set was processed using a retracker threshold of 5 % for sea-ice waveforms and the resulting sea-ice freeboard was calculated. In the next run, a fixed threshold of 10 % was used for all sea-ice waveforms and so on, until the last run with a sea-ice threshold of 95 % was computed and the resulting sea-ice freeboard was calculated.

From this data set, the optimal threshold, i.e., the threshold that yields the smallest difference in freeboard between Envisat RA-2 and CryoSat-2, was iteratively derived. An exemplary result is also shown in Figure 2-12. Again, also the optimal thresholds reflects the seasonal change in waveform parameters with a varying range of optimal threshold values that are in general higher for the early winter than the values in late winter.

● Oct ● Nov ● Dec ● Jan ● Feb ● Mar ● Apr

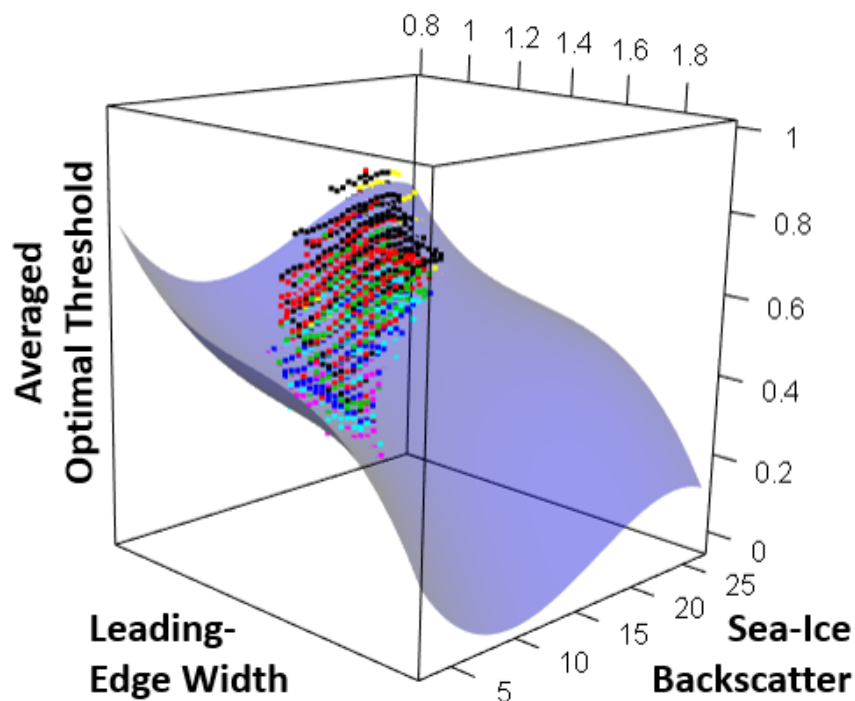


Figure 2-13: Visualizations of averaged binned optimal threshold values on an x-y plane of leading-edge width and sea-ice backscatter for the Arctic. The blue plane is the 3rd order polynomial fit through all data points

Next, average optimal threshold values were calculated for each 0.25 dB sea-ice backscatter and 0.025 leading-edge width bin on an x-y plane. A 3D visualization of this is shown in Figure 2-13. For months November through March both occurrences in the sensor overlap period were used. October and April, which were only covered once during the sensor overlap period were each added twice to circumvent issues of underrepresentation in their number of data values added to the total.

Through this compilation of monthly data points, three 3rd order polynomial planes were fitted based on different weighting schemes in order to maximize the adjusted R². As weights we used either the number of optimal threshold values per bin in the x-y plane, the inverse standard deviation of all optimal threshold values per bin ($1/\sigma$), or no weights at all.

For the Arctic, the result shown in Figure 2-13 is based on the inverse standard deviation as weights and achieved an adjusted R² of 0.94. All shown data points have a minimum of 50 occurrences and were obtained in the central Arctic only.

In Figure 2-13, the seasonal shift is also present: Early winter months tend towards shorter leading-edge widths and higher sea-ice backscatter values (October in yellow and November in Black), whereas late-winter months feature longer leading-edge widths and lower backscatter values.

The optimal threshold (th_{opt} ; in decimal values) to be used in the adaptive range retracking as a function of sea-ice backscatter (σ^0) and leading-edge width (lew) is given by the following equation:

$$th_{opt} = 3.4775697362 - 5.9296875486 \times lew + 4.3516498381 \times lew^2 - 1.0933131955 \times lew^3 - 0.0914747272 \times \sigma^0 + 0.0063983796 \times \sigma^{0^2} - 0.0001237455 \times \sigma^{0^3}$$

In a first attempt, we applied the same equation that was derived from the northern hemisphere data also to the southern hemisphere. However, this did not improve the results. The reason for that can partly be seen in Figure 2-14. In contrast to the Arctic, the differences between early and late winter is less prominent in the sea-ice freeboard differences as well as the optimal-threshold values. Additionally, patterns in sea-ice backscatter and leading-edge width are less correlated in some areas. This is potentially related to surface flooding and/or large fast-ice areas with a different snow stratigraphy.



Figure 2-14: As Figure 2-12 but for the Antarctic showing May 2011 (top row) and September 2011 (bottom row)

For the Antarctic, a 2nd order polynomial fit resulted in the best statistical result (adjusted R² of 0.77) to describe the optimal threshold as a function of leading-edge width and sea-ice backscatter (Figure 2-14).

For the Antarctic, the result shown in Figure 2-15 is based on the number of optimal threshold values per bin as weights. All shown data points also have a minimum of 50 occurrences and were obtained by excluding the marginal ice zones of the Antarctic as well as the austral summer months. However, compared to the Arctic, there is a much larger spread between months.

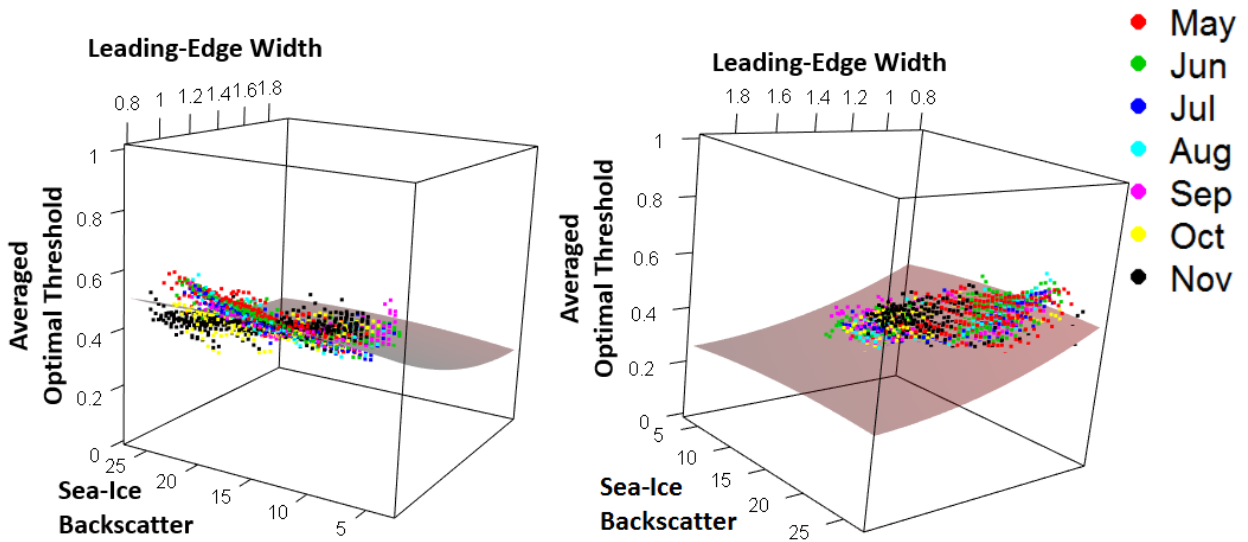


Figure 2-15: As Figure 2-13 but for the Antarctic and captured from two different viewpoints.

The equation to be used for deriving the optimal threshold (th_{opt} ; in decimal values) in the Antarctic adaptive range retracking as a function of sea-ice backscatter (σ^0) and leading-edge width (lew) is stated below:

$$th_{opt} = 0.8147895184 - 0.5555823623 \times lew + 0.1347526920 \times lew^2 + 0.0055934198 \times \sigma^0 - 0.0001431595 \times \sigma^{0^2}$$

Utilizing both equations, for each retracking of each sea-ice waveform, the to-be-used threshold is calculated from the waveform-associated sea-ice backscatter and leading-edge width value. This threshold is then believed to yield the mean-scattering surface in accordance to CryoSat-2 measurements.

2.5.2 Results

Here, we want to show and discuss some of the results using the adaptive threshold retracker for Envisat RA-2 in the sensor overlap period. For the Arctic, Figure 2-16 shows the average freeboard in centimeters per month, the average freeboard difference in centimeters as well as percent during the sensor overlap period for Envisat RA-2 and CryoSat-2. While in the first winter season, the match is nearly perfect with absolute average freeboard differences below one centimeter, the second winter season shows larger differences.

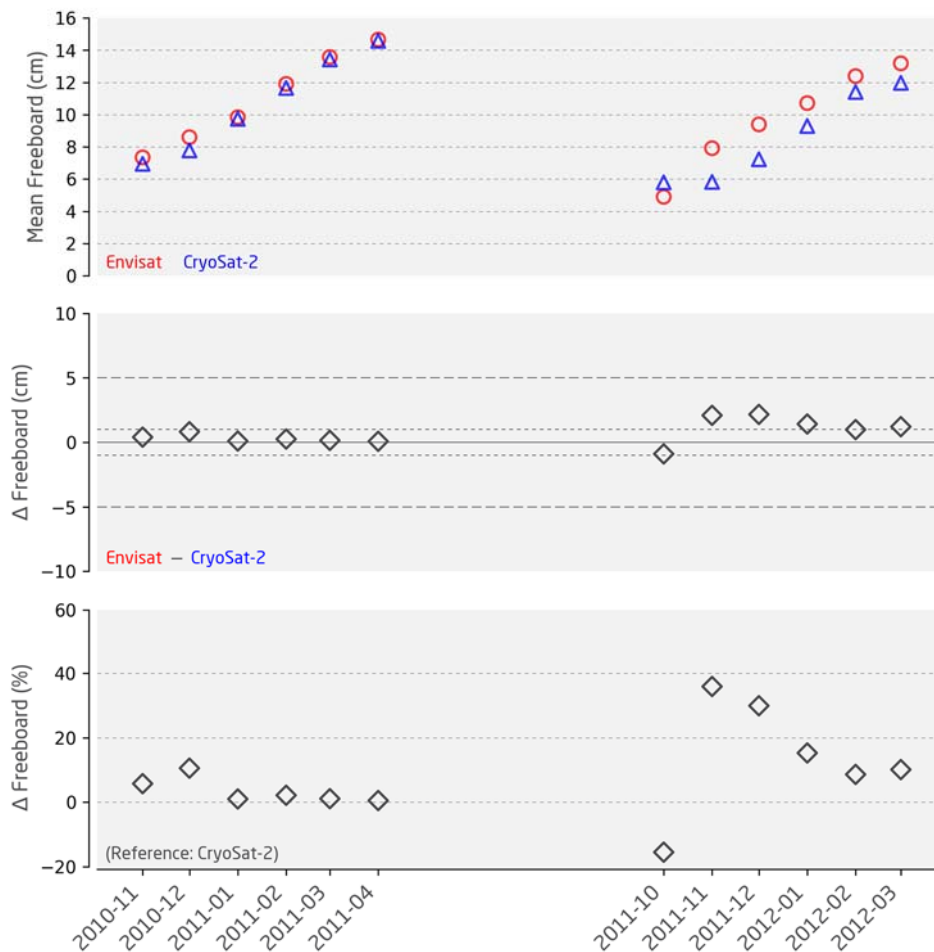


Figure 2-16: Mean freeboard for each month of the sensor overlap period (top) for Envisat RA-2 (red) and CryoSat-2 (blue) and the corresponding mean freeboard difference between both sensors in centimetres (middle) and percent with reference to CryoSat-2 (bottom) for the Arctic

However, these differences are still below three centimeters, which is a significant improvement over phase 1. Especially for the Arctic spring period (March & April), differences in average freeboard are 1.2 cm or better. The stability, i.e., the range of monthly differences, is 3.1 cm.

For the Antarctic, results are not as good as for the Arctic (Figure 2-17). Overall the algorithm has less skill to match Envisat RA-2 freeboards to the ones of

CryoSat-2. This is very likely related to other physical process such as more prominent snow stratigraphy and surface flooding. However, issues causing these differences are subject to further investigation. Overall, there is a stronger seasonality in the differences between summer and winter, which also leads toward a higher range of monthly differences of 4.6 cm.

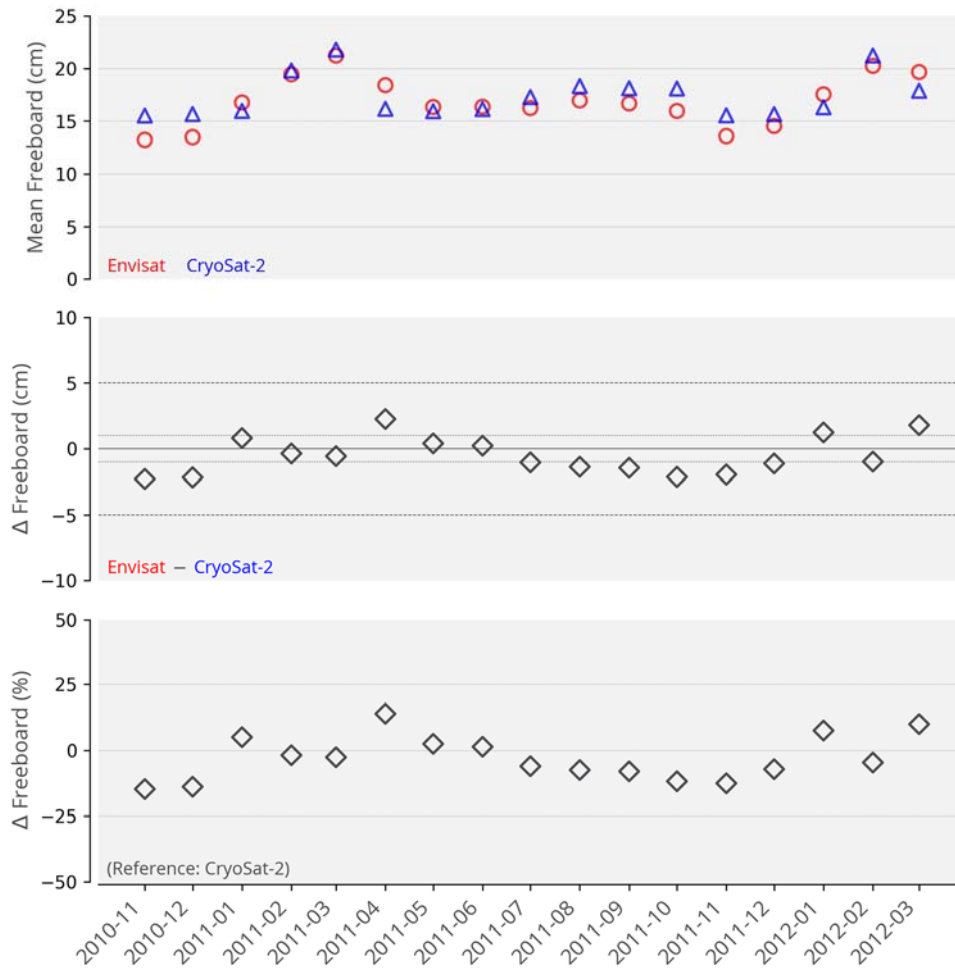


Figure 2-17: Setup as in Figure 2-16 but for the Antarctic

Putting all gridded freeboard values of Envisat RA-2 and CryoSat-2 against each other underlines these observations (Figure 2-18). While the algorithm is able to achieve very good agreement for the Arctic (Figure 2-18, left), the results are slightly more diffuse for the Antarctic (Figure 2-18, right).

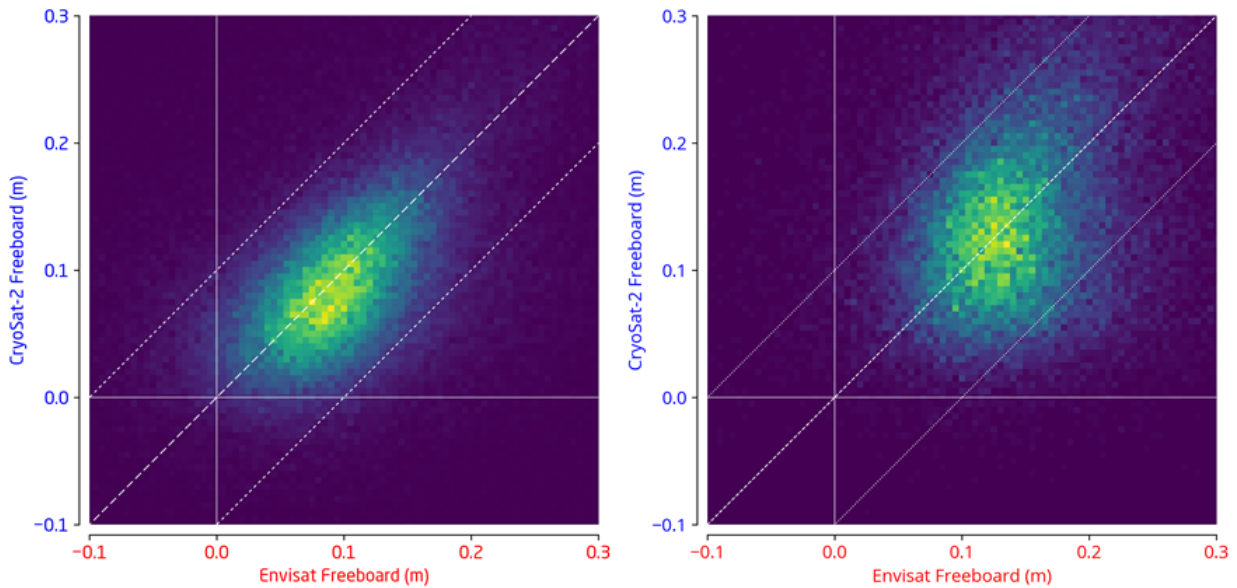


Figure 2-18: Scatterplot of all gridded freeboard estimates of CryoSat-2 (y-axis) vs. Envisat RA-2 (x-axis) for the Arctic (left) and the Antarctic (right).

2.6 Envisat Backscatter Drift Correction

Over the course of Envisat's life span, it appears that the RA-2 instrument has been degraded (Helm, 2017, pers. comm.). This results in a slight linear reduction in received backscatter over the years (Figure 2-19). As this can affect both the surface-type classification as well as the range retracking (as both are dependent on the received sea-ice backscatter), a correction had to be applied.

The monthly degradation factor of -0.003269253 was derived from the monthly averages of ocean-type waveforms in the Barents Sea (70°N-75°N and 40°E-50°E). Ocean-type waveforms are derived independent from the sea-ice backscatter classifier and we assume the surface roughness sufficiently random compared to ice-type waveforms for our analysis.

As the surface-type classification as well as the range retracking was derived from data in the sensor overlap period (November 2010 to March 2012), all backscatter values had to be corrected towards this base period. In order to accomplish that we picked June 2011 as a reference point.

Using the below given formula, we calculated the necessary backscatter drift correction:

$$t_{shift} = 12 \times (a_{ref} - a) + (m_{ref} - m)$$

$$\sigma_{drift}^0 = -0.003269253 \times t_{shift}$$

Here, t_{shift} is the time shift factor in months between the reference year (a_{ref}) and month (m_{ref}) and the currently processed year (a) and month (m). The resulting

backscatter drift correction (σ_{drift}^0) is then added to the sea-ice backscatter before the surface-type classification and the range retracking. By doing so, the in general slightly higher backscatter values during earlier years of Envisat's lifespan are reduced to the level during the sensor overlap period.

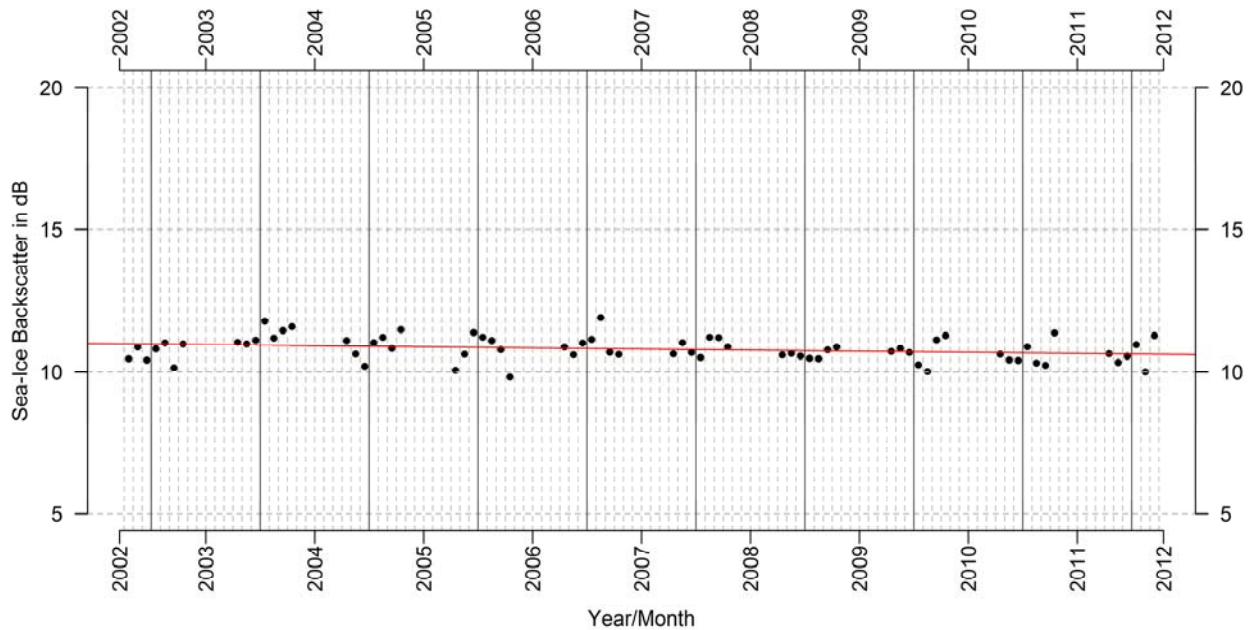


Figure 2-19: Visualizations of the monthly averaged sea-ice backscatter reduction between 2002 and 2012 over ocean-type waveforms obtained between 70°N-75°N and 40°E-50°E

2.7 Radar Freeboard, Sea-Surface Height and Sea-Ice Freeboard

The vast majority of the signal seen in the floe and lead elevations retracked in the last section is caused by unevenness in the Earth's gravity field and mean circulation of the ocean currents. This fixed signal known as the mean sea surface must be removed before any interpolation of the sea surface heights is attempted. Many models of the mean sea surface are available and there will almost certainly be one present in the satellite data product. It is however advisable to use a consistent mean sea surface height product based on altimeter data from the target period (1993-2016).

An example for such a global mean sea surface height product is DTU15 (Table 2-1), which is based on radar altimeter data from ERS-1 to CryoSat-2 and thus spans the target SIT ECV period and region. The DTU15 mean sea surface height is visualized in Figure 2-20.

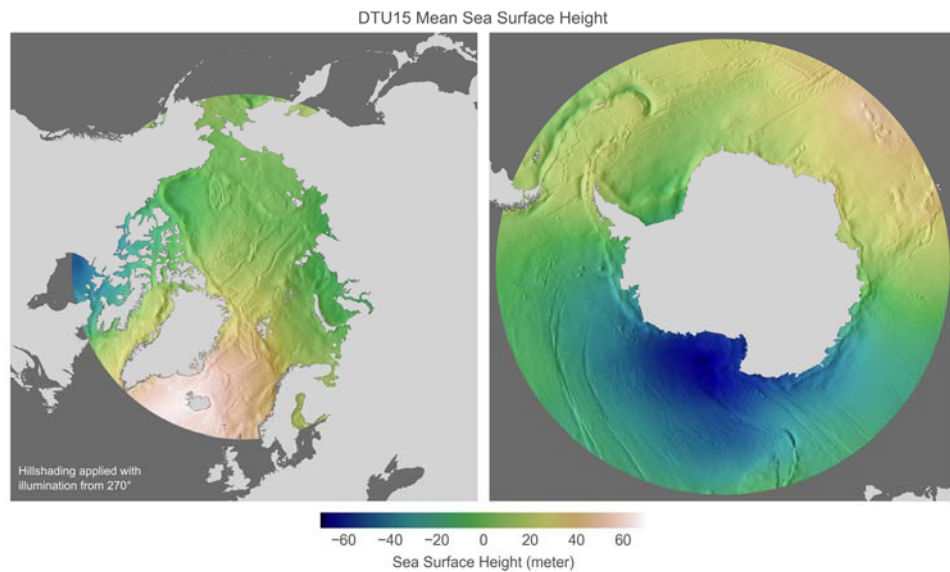


Figure 2-20: Hillshaded sea surface height of the DTU15 global mean sea surface height product for the SIT ECV target region in the northern and southern hemisphere

With the mean sea surface height removed from the sea surface heights in the leads, the remaining signal will be due to time variant changes in sea surface height caused by variability in the magnitude and direction of ocean currents; the dynamic topography and long wavelength errors in tides and atmospheric corrections. This signal varies on a scale of a few hundred kilometres. The ice freeboard, or the height the ice floe protrudes above the sea surface, is determined by interpolating the sea surface height beneath the floe location and subtracting it from the height of the floe. Figure 2-21 and Figure 2-22 illustrate this calculation. Practically, the residual of the lead elevations with respect to the mean sea surface height (MSSH) yield the sea surface height anomaly (SSHA). The instantaneous sea surface height (SSH) is then defined by

$$\text{SSH} = \text{MSSH} + \text{SSHA}$$

The sea surface height measurements are then linearly interpolated and smoothed by a box filter using a window size of 25 km. A minimum of one lead must exist for each orbit to allow a proper estimation of the instantaneous sea surface height. The result from subtracting the interpolated and smoothed sea-surface height from all retracked sea-ice elevations yields the radar freeboard. Radar freeboard in contrast to the sea-ice freeboard is not corrected for the slower wave propagation speed in the snow layer and therefore biased low.

In order to convert radar freeboard to sea-ice freeboard, a geometric correction has to be applied. For the Arctic, we use the Warren climatology [Warren et al., 1999] to retrieve snow thickness and snow depth values to calculate the correction factor. The Warren climatology is therefore scaled using the multi-year ice fraction data, as the climatology is strictly seen only valid over multi-year sea ice. However, the snow depth values are at least 50% of the original value over first-year sea ice. The sea-ice freeboard is then calculated by adding this scaled snow-depth value times the reduction factor of the wave-propagation speed in snow compared to the vacuum speed of light.

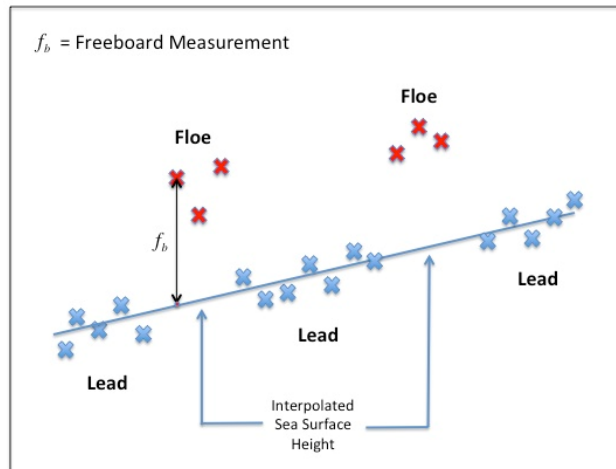


Figure 2-21: Computation of radar freeboard

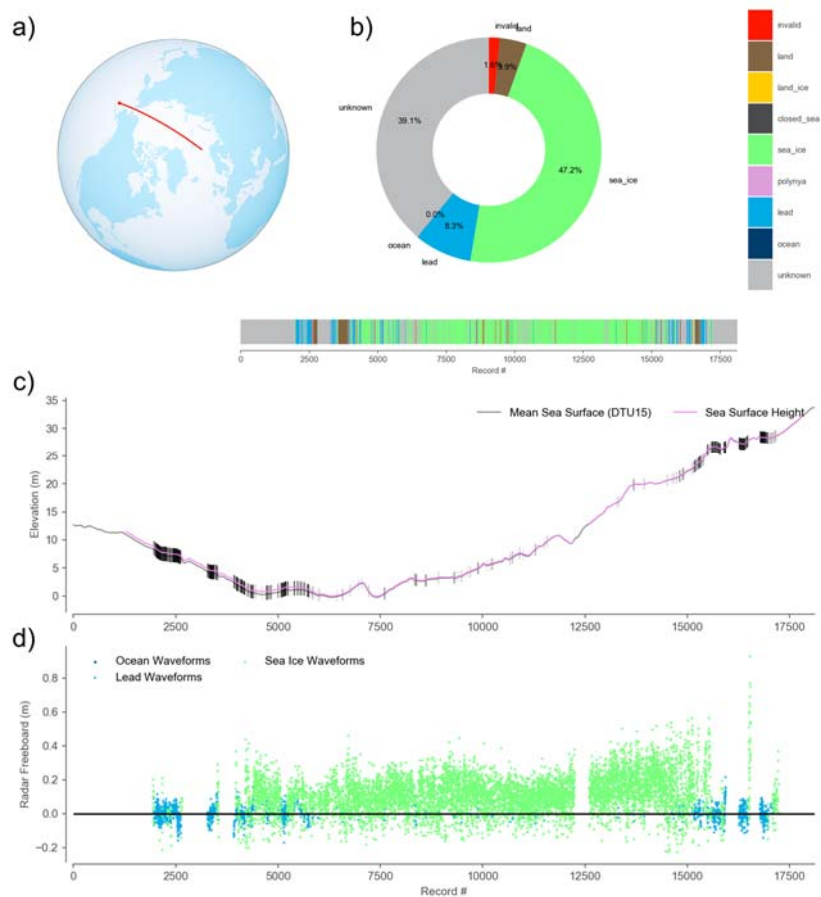


Figure 2-22: Example from along-track CryoSat-2 freeboard retrieval. a) Orbit location, b) surface type classification with classes unknown, lead and sea ice with percentage and geographical location along track c) Lead detections, mean sea surface height and sea surface height anomaly d) unfiltered radar freeboard

The procedure for the Antarctic is similar as for the Arctic, but we use the AMSR-E/2 snow-depth climatology provided by the ICDC.

Valid sea ice freeboards are assumed to range from 0 to 2 meter, while the range is extended by the range noise (0.25 meter) for individual footprint. Thus orbit data outside the range of -0.25 m to 2.25 meter is filtered.

2.8 Sea-Ice Thickness

The final step in the processing is to convert sea-ice freeboard to sea-ice thickness. The ice floe may or may not be covered by snow, but field studies have shown that if the floe is indeed snow covered the radar reflection and hence height measurement relate to the snow ice interface. This however may not always be the case as was shown by the laser / radar altimeter study in Fram Strait during the RRDP exercise. This most certainly is not the case for areas of seasonal sea ice, such as the Baltic Sea, for most of the winter. Thus freeboard values should be understood as "altimeter freeboard" values. That is, for the cold central Arctic they can be assumed to represent the ice freeboard, but for marginal areas the elevation measured is somewhere between the ice and snow freeboard. But since this effect cannot be parameterized with available EO observations, it is always assumed in the processing that the dominant reflector is the snow/ice interface.

Since the ice floe is in isostatic equilibrium, a simple calculation using freeboard and snow depth, and the densities of snow, sea ice and sea water, can be used to compute the thickness. Figure 2-23 illustrates this calculation. The final thickness is given by:

$$z_i = \frac{z_s \rho_s + f_b \rho_w}{\rho_w - \rho_i}$$

Where:

z_i = Sea-ice thickness. z_s = Snow depth. f_b = Sea-ice freeboard.

ρ_s = Snow density. ρ_w = Density of sea water. ρ_i = Density of sea ice.

In the Arctic, the snow depth and density are obtained from the Warren climatology [Warren et al., 1999]. Since the snow depth measurements contributing to the Warren climatology originate exclusively from multi-year ice, the snow depth values are similarly scaled as for the snow geometric correction applied for the derivation of sea-ice freeboard from radar freeboard. As the Warren climatology is valid only in the central Arctic, we have to mask out measurements where it yields unreliable results ($0.0 < \text{snow depth} < 0.6$). This usually leads to masking of areas, for example Baffin Bay and the Baltic Sea in some months. We also follow the approach to scale the snow depth with the MYI fraction, leading to a 50% reduction of snow depth in FYI dominated regions. We only apply the MYI fraction scaling to snow depth and not density, as the latter is only marginally dependant on sea ice type.

For water density we use the fixed values of 1024 kg/m³. Direct measurements of sea ice density suggest that the density of multi-year ice is less than that of first-

year ice. We therefore use a parameterization of the sea ice density that is scaled by the multi-year ice fraction between the density of multi-year ice (882 kg/m^3) and first-year ice (916.7 kg/m^3).

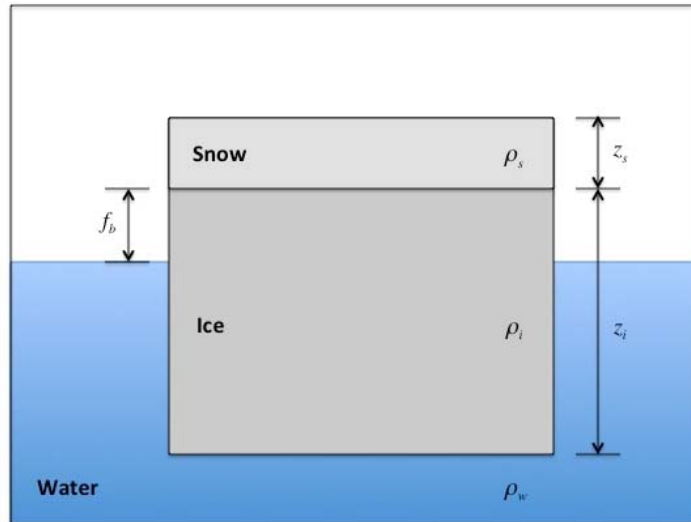


Figure 2-23: Computation of sea-ice thickness

2.9 Uncertainties

The computation of product uncertainties is based on the error propagation of the input parameters uncertainties. Input parameter uncertainties are either obtained directly from the auxiliary data products or based on assumptions. Exempt from the uncertainty computations are the sea ice concentration (sic) values used for surface type classification and the mean sea surface (mss), where no uncertainty estimation is available.

The uncertainty computation is estimated for each point independently and thus available at the same resolution as the freeboard/thickness values in the Level-2 product. The usage of error propagation is based on the assumption that all error components are uncorrelated, which might not always be the case for sea ice. Without the knowledge of the covariance of all error components we need to utilize this first order approximation.

Table 2-8: Overview of uncertainty sources for sea ice freeboard and thickness retrieval

Parameter	Envisat		CryoSat-2	
	Arctic	Antarctic	Arctic	Antarctic
Radar Range (Elevation)	0.15m	0.15m	0.1m	0.1m
Sea Surface Height	computed (see below)			
Sea Ice Type	product	10%	product	10%
Snow Depth	Warren99	product	Warren99	product
Snow Density	Warren99	20 kg/m^3	Warren99	20 kg/m^3
Radar Freeboard	computed (see below)			

Parameter	Envisat		CryoSat-2	
Freeboard	computed (see below)			
Sea Ice Density	computed (see below)			
Sea Water Density	0 kg/m ³	0 kg/m ³	0 kg/m ³	0 kg/m ³
Sea Ice Thickness	computed (see below)			

Table 2-8 show an overview of the uncertainty components which are set to fixed values, taking from an auxiliary data product or computed.

2.9.1 Sea Surface Height Uncertainty

The uncertainty of the sea surface height depends on the base ssh uncertainty and the distance to the closest sea surface height tie point. The values for base ssh uncertainty is assumed to be 2 cm to include effects such as leads covered with thin ice and the maximum uncertainty is assumed as 10 cm based on investigations of the typical variation of the anomaly between the instantaneous sea surface height and mean sea surface along polar crossing orbits.

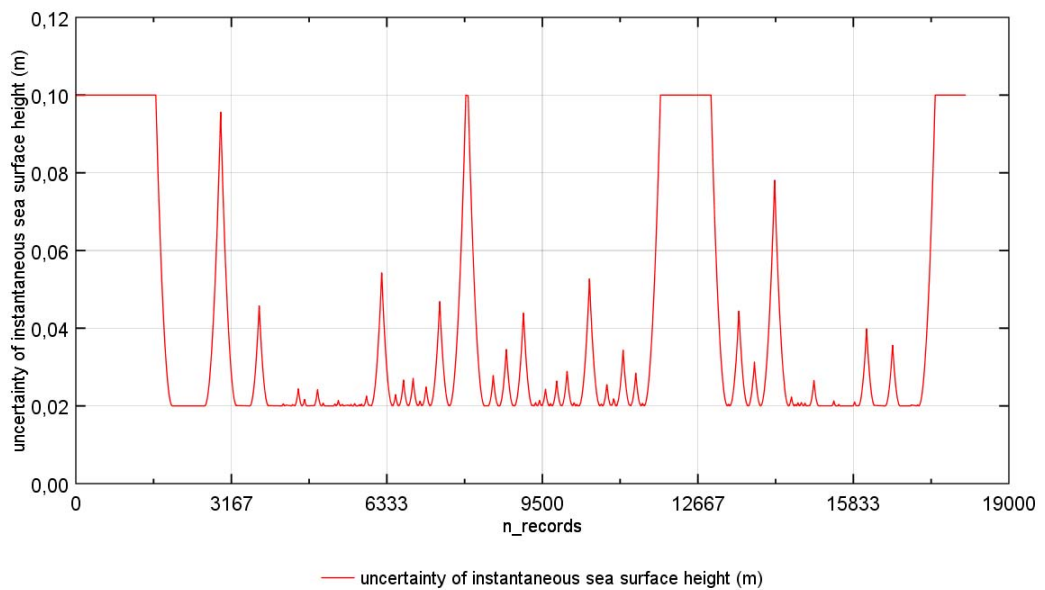


Figure 2-24: Example of Sea Surface Height Uncertainty

The sea surface height uncertainty is computed as

$$\sigma_{ssh} = \begin{cases} 0.02m + 0.1m \times \left(\frac{d_{tp}}{100km} \right)^2, & d_{tp} < 100km \\ 0.1m, & d_{tp} \geq 100 km \end{cases}$$

With d_{tp} as the distance to the next sea surface height tie point.

2.9.2 Radar Freeboard Uncertainty

The radar freeboard uncertainty is computed by error propagation of the range or elevation uncertainty and the sea surface height uncertainty. For the simple case of radar freeboard being the difference between elevation and sea surface height, the radar freeboard uncertainty is given by:

$$\sigma_{rfrb} = \sqrt{\sigma_{elev}^2 + \sigma_{ssh}^2}$$

The elevation uncertainty σ_{elev} are fixed assumptions based on noise estimations for Envisat RA-2 und CryoSat-2 SIRAL sensors (See Table 2-8).

2.9.3 Sea Ice Type (MYI Fraction) Uncertainty

In the Arctic the myi fraction uncertainty (σ_{fmyi}) is taken directly from the MYI fraction product (field `my_sea_ice_area_fraction_sdev`)

No sea ice type product is available in the Antarctic and the general assumption is that all sea ice can be described as FYI. Nevertheless we assume a static uncertainty of 10% for the MYI fraction to account for sea ice type based uncertainties.

2.9.4 Snow Depth Uncertainty

The Uncertainty of snow depth is taken from the input auxiliary data sets. In the case of the Arctic we use the information of inter-annual variability as an estimation for snow depth uncertainty. Since the snow depth (sd) is however modified by the myi fraction, the uncertainty of the snow depth is also scaled on MYI fraction (f_{myi}) (50% of the original value for FYI and 100% for MYI respectively).

We also include an additional term that represents the effect myi fraction uncertainty on the scaling assumption between FYI and MYI snow depth:

$$(Arctic) \quad \sigma_{sd} = \underbrace{f_{myi} \times \sigma_{sd}^{W99}}_{Scaled\ W99\ Uncertainty} + \underbrace{sd \times (1 - f_{myi}) \times \sigma_{fmyi}}_{Scaling\ Uncertainty}$$

In the southern hemisphere the field `mediansnowdepth_filtered100_variability` of the snow depth climatology product is used as uncertainty estimate.

2.9.5 Snow Density Uncertainty

In the Arctic the snow density uncertainty (σ_{ρ}^s) is provided by the Warren climatology as well. The difference in sea ice density between FYI and MYI is

small, therefore the snow density and its uncertainty are assumed to be independent from the myi fraction.

In the Antarctic, we assume a fixed uncertainty of 20 kg/m³.

2.9.6 Freeboard Uncertainty

In addition to the radar freeboard uncertainty, the freeboard uncertainty needs to take the component introduced by the snow wave speed correction into accounts. While the wave speed reduction is assumed to be reasonably well known, the additional uncertainty is controlled by snow depth (*sd*) uncertainty (σ_{sd}).

$$\sigma_{frb} = \sqrt{(sd \times \sigma_{sd})^2 + \sigma_{rfrb}^2}$$

2.9.7 Sea Ice Density Uncertainty

Similar to snow depth, sea ice density (ρ_i) is a parameter obtained by scaling between the values for FYI and MYI using the myi fraction. To estimate the uncertainty (σ_{ρ}^i), we scale between the uncertainties of FYI density (σ_{ρ}^{fyi}) and MYI density (σ_{ρ}^{myi}) and add a term for the scaling uncertainty.

$$\sigma_{\rho}^i = \underbrace{\sigma_{\rho}^{fyi} + f_{myi} \times (\sigma_{\rho}^{myi} - \sigma_{\rho}^{fyi})}_{\text{Uncertainty Scaling}} + \underbrace{\sigma_{fmyi} \times (\sigma_{\rho}^{fyi} - \sigma_{\rho}^{myi})}_{\text{Scaling Uncertainty}}$$

2.9.8 Sea Ice Thickness Uncertainty

The sea ice thickness uncertainty is computed as the error propagation of the input uncertainties.

$$\sigma_{sit} = \sqrt{\left(\frac{\rho_w}{\rho_w - \rho_i} \sigma_{frb}\right)^2 + \left(\frac{frb \cdot \rho_w + sd \cdot \rho_i}{\rho_w - \rho_i} \sigma_{\rho}^i\right)^2 + \left(\frac{\rho_s}{\rho_w - \rho_i} \sigma_{sd}\right)^2 + \left(\frac{sd}{\rho_w - \rho_i} \sigma_{\rho}^s\right)^2}$$

2.9.9 Level-3 Gridded Uncertainties

The Level-3 product contains the average uncertainties for freeboard/thickness respectively per grid cell to reflect that the biggest uncertainty components, e.g. snow depth, sea ice density, retracker biases, are not random uncertainties that would be reduced by averaging. This approach will therefore result in overestimating of the true uncertainty in the Level-3 product, but will remain more realistic in grid cell with many data points.

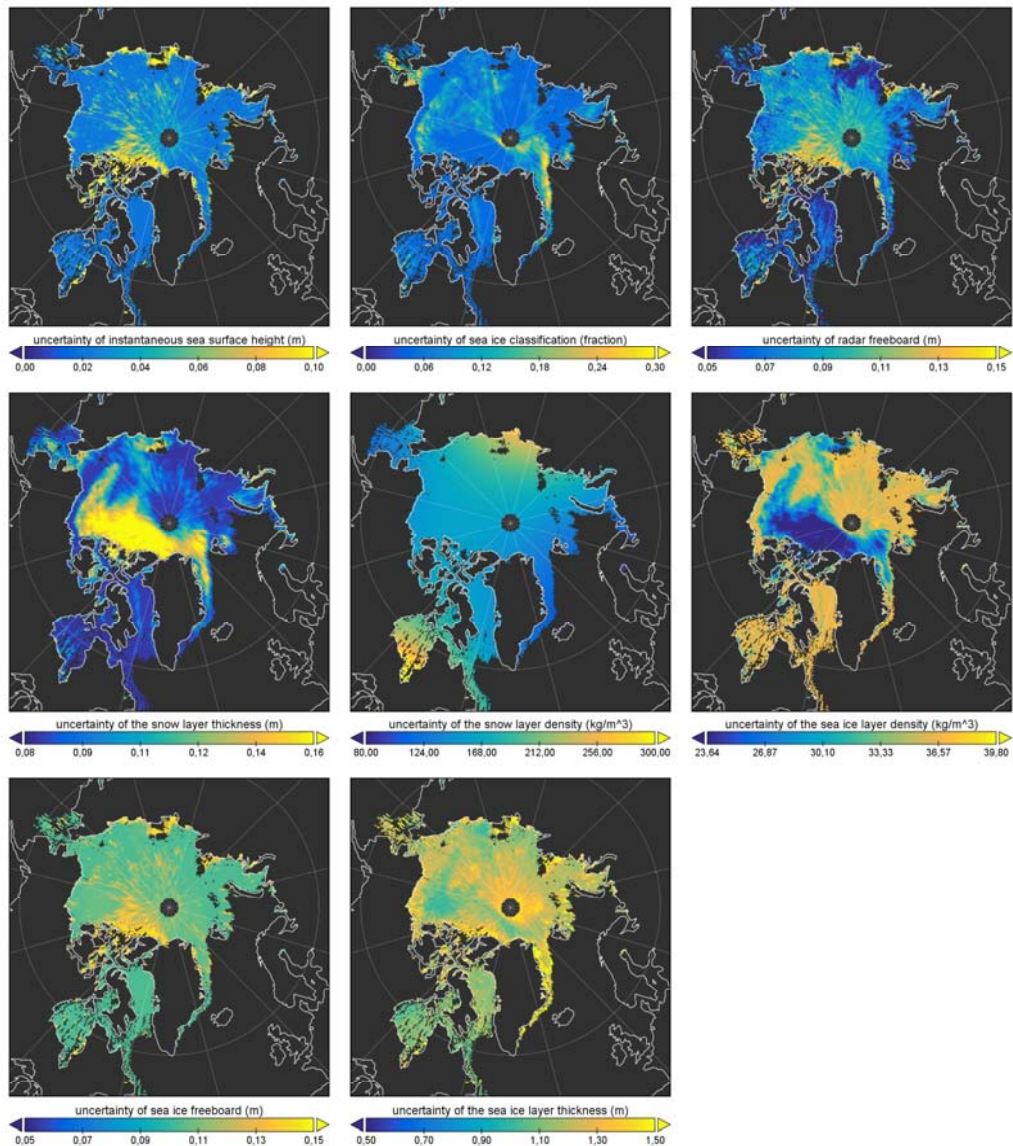


Figure 2-25: Gridded uncertainties (Example CryoSat-2 March 2015 Arctic data)

3 References

Andersen, S., Tonboe, R., Kaleschke, L., Heygster, G., and Pedersen, L. T.: Intercomparison of passive microwave sea ice concentration retrievals over the high-concentration Arctic sea ice, *JOURNAL OF GEOPHYSICAL RESEARCH*, 112, 2007.

Andersen, S., Tonboe, R., Kern, S., and Schyberg, H.: Improved retrieval of sea ice total concentration from spaceborne passive microwave observations using numerical weather prediction model fields: An intercomparison of nine algorithms, *Remote Sensing of Environment*, 104, 374-392, 2006.

Andersen, S.: Monthly Arctic Sea Ice Signatures for use in Passive Microwave Algorithms, TECHNICAL REPORT 98-18 DANISH METEOROLOGICAL INSTITUTE, 1998.

ARCGICE: Combination of Spaceborne, Airborne and In-Situ Gravity Measurements in Support of Arctic Sea-Ice Thickness Mapping, (2007). ESA Contract 18753/05/NL/CB.

Bjoergo, E., Johannessen, O. M., and Miles, M. W.: Analysis of merged SMMR-SSM/I time series of Arctic and Antarctic sea ice parameters 1978-1995, *Geophysical Research Letters*, 24, 1997.

Breiman, L.: Random Forests, *Machine Learning*, 45, 5-32, <https://doi.org/10.1023/A:1010933404324>, 2001.

Cavalieri, D. J., T. Markus, and J. C. Comiso. 2014. *AMSR-E/Aqua Daily L3 12.5 km Brightness Temperature, Sea Ice Concentration, & Snow Depth Polar Grids*. Version 3. June 2002 – October 2011. Boulder, Colorado USA: NASA National Snow and Ice Data Center Distributed Active Archive Center. doi: http://dx.doi.org/10.5067/AMSR-E/AE_SI12.003.

Cavalieri, D. J., Germain, K. S., and Swift, C. T.: Reduction of weather effects in the calculation of sea ice concentration with the DMSP SSM/I, *J. Glaciol.*, 41, 1995.

Cavalieri, D. J., Gloersen, P., and Campbell, W. J.: Determination of Sea Ice Parameters With the NIMBUS 7 SMMR, *Journal of Geophysical Research*, 89, 5355-5369, 1984.

Cavalieri, D.J., C.L. Parkinson, P. Gloersen, J.C. Comiso, and H.J. Zwally. Deriving long-term time series of sea ice cover from satellite passive-microwave multisensor data sets. *Journal of Geophysical Research* 104(C7), 15803-15814, 1999.

Comiso, J. C., and Sullivan, C. W.: Satellite Microwave and In Situ Observations of the Weddell Sea Ice Cover and its Marginal Ice Zone, *Journal of Geophysical Research*, 91, 9663-9681, 1986.

Comiso, J. C., Cavalieri, D. J., Parkinson, C. L., and Gloersen, P.: Passive Microwave Algorithms for Sea Ice Concentration: A Comparison of Two Techniques, *Remote Sensing of Environment*, 60, 357-384, 1997.

Comiso, J. C.: Characteristics of Arctic Winter Sea Ice From Satellite Multispectral Microwave Observations, *Journal of Geophysical Research*, 91, 975-994, 1986.

Comiso, J. C.: SSM/I Sea Ice Concentrations Using the Bootstrap Algorithm, NASA Reference Publication / Goddard Space Flight Center, 1380, 1995.

Eastwood, S. (editor): Ocean & Sea Ice SAF (OSISAF) Sea Ice Product Manual. Version 3.8. May 2012

Emery, W. J., Fowler, C., and Maslanik, J.: Arctic sea ice concentrations from special sensor microwave imager and advanced very high resolution radiometer satellite data, *Journal of Geophysical Research*, 99, 18329 - 18342, 1994.

European Space Agency Envisat RA-2/MWR Product Handbook, Issue2.2, 27 February 2007. Available for download from <http://envisat.esa.int/handbooks>.

Giles, K. A., Laxon, S. W., Wingham, D. J., Wallis, D. W., Krabill, W. B., Leuschen, C. J., McAdoo, D., Manizade, S. S., & Raney, R. K. (2007). Combined airborne laser and radar altimeter measurements over the Fram Strait in May 2002. *Remote Sensing of Environment* 111 182 - 194.

Gloersen, P., and Cavalieri, D. J.: Reduction of Weather Effects in the Calculation of Sea Ice Concentration From Microwave Radiances, *Journal of Geophysical Research*, 91, 1986.

Hartigan, J. A. and Wong, M. A.: Algorithm AS 136: A K-Means Clustering Algorithm, 28, 100-108, <http://www.jstor.org/stable/2346830>, 1979.

Ivanova, N., Johannessen, O. M., Pedersen, L. T., and Tonboe, R. T.: Retrieval of Arctic Sea Ice Parameters by Satellite Passive Microwave Sensors: A Comparison between Eleven Sea Ice Concentration Algorithms, submitted to *IEEE Transactions on Geoscience and Remote Sensing*, 2013.

Kaleschke, L., Lupkes, C., Vihma, T., Haarpaintner, J., Bochert, A., Hartmann, J., and Heygster, G.: SSM/I Sea Ice Remote Sensing for Mesoscale Ocean-Atmosphere Interaction Analysis, *Canadian Journal of Remote Sensing*, 27, 526-537, 2001.

JAXA-EORC (Japan Aerospace Exploration Agency, Earth Observation Research Center), 2015: Status of AMSR2 Level-1 Products (Ver. 2.0).

Kattsov, V. M., Ryabinin, V. E., Overland, J. E., Serreze, M. C., Visbeck, M., Walsh, J. E., Meier, W., and Zhang, X.: Arctic sea-ice change: a grand challenge of climate science, *Journal of Glaciology*, 56, 2010.

Kern, S., and G. Heygster (2001), Sea ice concentration retrieval in the Antarctic based on the SSM/I 85 GHz polarization, *Annals of Glaciology*, 33, 109-114.

Kongoli, C., Boukabara, S.-A., Banghua Yan, F. W., and Ferraro, R.: A New Sea-Ice Concentration Algorithm Based on Microwave Surface Emissivities—Application to AMSU Measurements, *IEEE Transactions on Geoscience and Remote Sensing*, 2010.

Kurtz, N. T., and S. L. Farrell. Large-scale surveys of snow depth on Arctic sea ice from Operation IceBridge. *Geophysical Research Letters*, 38, L20505, 2011. doi: 10.1029/2011GL049216.

Laxon, S. W., Peacock, N. R. & Smith, D. M. (2003). High interannual variability of sea ice thickness in the Arctic region. *Nature*, doi:10.1038/nature2050, 947-950.

Lo, R. C.: A comprehensive description of the Mission Sensor Microwave Imager SSM/I environmental parameter extraction algorithm. NRL Memorandum Report 5199, Naval Research Laboratory, Washington D. C., 1983.

Maass, N., & Kaleschke, L. (2010). Improving passive microwave sea ice concentration algorithms for coastal areas: applications to the Baltic Sea. *Tellus Series A-Dynamic Meteorology and Oceanography*, 62(4), 393-410.

Markus, T. and D.J.Cavalieri. Snow Depth Distribution over Sea Ice in the Southern Ocean from Satellite Passive Microwave Data. *Antarctic Sea Ice: Physical Processes, Interactions and Variability, Antarctic Research Series*, 74, 19-39, 1998.

Markus, T., and Cavalieri, D. J.: An Enhancement of the NASA Team Sea Ice Algorithm, *IEEE Transactions on Geoscience and Remote Sensing*, 38, 2000.

MacQueen, J.: Some methods for classification and analysis of multivariate observations, 1967.

Meier, W., F. Fetterer, K. Knowles, M. Savoie, M. J. Brodzik. (2006, updated quarterly). Sea Ice Concentrations from Nimbus-7 SMMR and DMSP SSM/I-SSMIS Passive Microwave Data, 2002 until present. Boulder, Colorado USA: National Snow and Ice Data Center. *Digital Media*.

Peacock, N. R. & Laxon, S. W. (2004) Sea surface height determination in the Arctic Ocean from ERS altimetry. *Journal of Geophysical Research*, Vol. 109, No. C7, C07001 10.1029/2001JC001026.

Pedersen, L. T.: Improved spatial resolution of SSM/I products. In: Sandven, S., ed. Development of new satellite ice data products, Nansen Environmental and Remote Sensing Center, Bergen, Norway, 1998.

Pedersen, L. T.: Retrieval of sea ice concentration by means of microwave radiometry. The Technical University of Denmark, 1991.

Ramseier, R. O.: Sea Ice Validation. In: Hollinger, J. P., ed. DMSP special sensor microwave/imager calibration/validation, Naval Research Laboratory, Washington, DC, 1991.

Ramseier, R., Rubinstein, I. G., and Davies, A. F.: Operational evaluation of Special Sensor Microwave/Imager by the Atmospheric Environment Service, report from the Centre for Research in Experimental Space Science, York University, North York, Ontario, Canada, 1988.

Ricker, R., Hendricks, S., Helm, V., Skourup, H., and Davidson, M.: Sensitivity of CryoSat-2 Arctic sea-ice freeboard and thickness on radar-waveform interpretation, *The Cryosphere*, 8, 1607-1622, doi:10.5194/tc-8-1607-2014, 2014.

Rinne, E., and M. Mäkynen. Sea Ice Thickness Round-Robin Data Package: User Manual. ESA Sea Ice Climate Change Initiative: Phase 1, NERSC. Version 1.2, 2013 (access 23.3.2016).

Shokr, M., Lambe, A., and Agnew, T.: A New Algorithm (ECICE) to Estimate Ice Concentration From Remote Sensing Observations: An Application to 85-GHz

Passive Microwave Data, IEEE Transactions on Geoscience and Remote Sensing, 46, 2008.

Smith, D. M., and Barrett, E. C.: Satellite mapping and monitoring of sea ice. Unpublished final report to the Defence Research Agency, RSU, University of Bristol, 1994.

Smith, D. M.: Extraction of winter total sea-ice concentration in the Greenland and Barents Seas from SSM/I data, International Journal of Remote Sensing, 17, 2625 - 2646, 1996.

Spreen, G. Meereisfernerkundung mit dem satellitengestützten Mikrowellenradiometer AMSR(-E) – Bestimmung der Eiskonzentration und Eiskante unter Verwendung der 89 Ghz-Kanäle. Diploma Thesis, University of Hamburg, prepared at the University of Bremen, Department of Physics and Electrical Engineering, 2004.

Spreen, G., Kaleschke, L., and Heygster, G.: Operational Sea Ice Remote Sensing with AMSR-E 89GHz Channels, IEEE International Geoscience and Remote Sensing Symposium Proceedings, 6, 4033-4036, 2005.

Spreen, G., L. Kaleschke, and G. Heygster. Sea Ice Remote Sensing Using AMSR-E 89 GHz Channels. *Journal of Geophysical Research*, 113, C02S03, doi:10.1029/2005JC003384, 2008.

Steffen, K., Cavalieri, D. J., Comiso, J. C., Germain, K. S., Gloersen, P., and Rubinstein, I.: The estimation of geophysical parameters using passive microwave algorithms. In: Carsey, F., ed. *Microwave Remote Sensing of Sea Ice*, American Geophysical Union, Washington, DC, 1992.

Svendsen, E., Kloster, K., Farrelly, B., Johannessen, O. M., Johannessen, J. A., Campbell, W. J., Gloersen, P., Cavalieri, D., and Matzler, C.: Norwegian Remote Sensing Experiment' Evaluation of the Nimbus 7 Scanning Multichannel Microwave Radiometer for Sea Ice Research, *Journal of Geophysical Research*, 88, 2781-2791, 1983.

Svendsen, E., Matzler, C., and Grenfell, T.: A model for retrieving total sea ice concentration from a spaceborne dual-polarized passive microwave instrument operating near 90 GHz, *International Journal of Remote Sensing*, 8, 1479 - 1487, 1987.

Swift, C., Fedor, L., and Ramseier, R.: An Algorithm to Measure Sea Ice Concentration With Microwave Radiometers, *Journal of Geophysical Research*, 90, 1985.

Tikhonov, V. V., I.A. Repina, M.D. Raev, E.A. Sharkov, V.V. Ivanov, D.A. Boyarskii, T.A. Alexeeva, N.Yu. Komarova, A physical algorithm to measure sea ice concentration from passive microwave remote sensing data, *Advances in Space Research*, Volume 56, Issue 8, 15 October 2015, Pages 1578-1589, ISSN 0273-1177, <http://dx.doi.org/10.1016/j.asr.2015.07.009>.

Walters, J. M., Ruf, C., and Swift, C. T.: A Microwave Radiometer Weather-Correcting Sea Ice Algorithm, *Journal of Geophysical Research*, 92, 1987.

Warren, S. G., Rigor, I. G., Untersteiner, N., Radionov, V. F., Bryazgin, N. N., Aleksandrov, Y. I., et al. (1999). Snow depth on Arctic sea ice. *Journal of Climate*, 12

Wentz, F. J. A well-calibrated ocean algorithm for SSM/I. *Journal of Geophysical Research* 102(C4), 8703-8718, 1997.

Wentz, F. J. and T. Meissner. AMSR Ocean Algorithm, Version 2, vol. 121599A-1, p. 66, Remote Sensing Systems, Santa Rosa, CA, 2000.

Wiebe, H., G. Heygster and L. Meyer-Lerbs 2008: Geolocation of AMSR-E Data. *IEEE Trans. Geosci. and Remote Sensing* 46(10), p. 3098-3103, doi:10.1109/TGRS.2008.919272.

Xiaolong Dong, Ke Xu, Huguang Liu, Jingshan Jiang 2004: The radar altimeter and scatterometer of China's HY-2 satellite, IGARSS '04. *Proceedings. 2004 IEEE International 2004* 10.1109/IGARSS.2004.1370659

< End of Document >